Light absorption properties and potential sources of particulate brown carbon in the Pearl River Delta region of China

Zhujie Li[1,2], Haobo Tan[2]*, Jun Zheng[1]*, Li Liu[2,3], Yiming Qin[4], Nan Wang[2], Fei Li[2], Yongjie Li[5], Mingfu Cai[3], Yan Ma[1], and Chak K. Chan[4]

[1]Collaborative Innovation Center of Atmospheric Environment and Equipment Technology, Nanjing University of Information Science and Technology, Nanjing, China

[2]Key Laboratory of Regional Numerical Weather Prediction, Institute of Tropical and Marine Meteorology, China Meteorological Administration, Guangzhou, China

[3]Department of Atmospheric Science, Sun yat-sen University, Guangzhou, China

[4]School of Energy and Environment, City University of Hong Kong, Hong Kong, China

[5]Department of Civil and Environmental Engineering, Faculty of Science and Technology, University of Macau, Macau, China

Correspondence to: Haobo Tan (hbtan@grmc.gov.cn) and Jun Zheng (zheng.jun@nuist.edu.cn)

19 **Abstract:**

20 Brown carbon (BrC) is a special type of organic aerosols (OA), capable of absorbing solar

21 radiation from near-ultraviolet (UV) to visible wavelengths, which may lead to an increased

22 aerosol radiative effect in the atmosphere. While high concentrations of OAs have been

23 observed in the Pearl River Delta (PRD) region of China, the optical properties and

24 corresponding radiative forcing of BrC in the PRD are still not well understood. In this work,

25 we conducted a set of comprehensive measurements of atmospheric particulate matter from 29

26 November 2014 to 2 January 2015 to investigate aerosol compositions, optical properties,

27 source origins and radiative forcing effects at a suburban station in Guangzhou. The particle

28 absorption Ångström exponent (AAE) was deduced and utilized to differentiate light absorption

29 by BrC from that by black carbon (BC). The results showed that the average absorption

30 contributions of BrC were 34.1±8.0% at 370 nm, 23.7±7.3% at 470 nm, 16.0±6.7% at 520 nm,

31 13.0±5.4% at 590 nm and 8.7±4.3% at 660 nm. A sensitivity analysis of the evaluation of the

32 absorption Ångström exponent of BC (AAE_{BC}) was conducted based on the Mie theory

33 calculation assuming that the BC-containing aerosol was mixed with the core-shell and external

34 configurations. The corresponding uncertainty in AAE_{BC} was acquired. We found that

35 variations in the imaginary refractive index (RI) of the BC core can significantly affect the

36 estimation of AAE_{BC}. However, AAE_{BC} was relatively less sensitive to the real part of the RI

37 of the BC core and was least sensitive to the real part of the RI of the nonlight absorbing shell.

38 BrC absorption was closely related to aerosol potassium cation content (K^+), a common tracer

39 of biomass burning emissions, which was most likely associated with straw burning in the rural

40 area of the western PRD. Diurnal variation in BrC absorption revealed that primary organic

41 aerosols had a larger BrC absorption capacity than secondary organic aerosols (SOAs).

42 Radiative transfer simulations showed that BrC absorption may cause 2.3±1.8 W m^{-2} radiative

43 forcing at the top of the atmosphere (TOA) and contribute to 15.8±4.4% of the aerosol warming

44 effect. A chart was constructed to conveniently assess the BrC radiative forcing efficiency in

45 the studied area with reference to certain aerosol single-scattering albedo (*SSA*) and BrC

46 absorption contributions at various wavelengths. Evidently, the BrC radiative forcing efficiency

47 was higher at shorter wavelengths.

Keywords: Brown carbon, Black carbon, Absorption Ångström exponent, Radiative forcing, Pearl River Delta.

48 **1 Introduction**

49 Black carbon (BC) and organic carbon (OC) are dominant carbonaceous aerosol components

50 that mainly originate from biomass burning in a global scale (Bond et al., 2004) and have

51 attracted great environmental concerns in rapidly developing regions. Carbonaceous aerosols

52 can not only exert adverse impacts on public health, similar to other particulate matters, but

53 also significantly affect the terrestrial radiation balance with enormous uncertainties. In

54 previous studies, BC was often considered to be the only light-absorbing species (Andreae and

55 Gelencser, 2006), and OC was believed to only be able to scatter light, i.e., causing a cooling

56 effect (Bond et al., 2011). Nevertheless, it has been reported that some fraction of organic

57 aerosols (OAs) may also specifically contribute to light absorption from the near-ultraviolet

58 (UV) to visible wavelength range, which is referred to as brown carbon (BrC) (Kirchstetter et

59 al., 2004). BrC optical properties are strongly affected by its chemical composition and physical

60 structure, which are related to different BrC sources. BrC can originate not only from direct

61 emissions, including smoldering, biomass burning or any type of incomplete fuel combustion

62 process (T. C. Bond et al., 1999;Cheng et al., 2011), but also from secondary organic aerosol

63 formation processes, such as aqueous phase reactions in acidic solutions (Desyaterik et al., 2013)

64 or volatile organic compound (VOC) oxidation (Laskin et al., 2015;Sareen et al., 2010). In

65 addition, BrC could have a complicated molecular composition and intermix with other

66 substances, such as BC, non-absorbing OAs and other inorganic materials, making it

67 complicated to investigate BrC optical properties.

68 BC absorption is commonly assumed to be covering the full wavelength-range. However, the

69 light absorption property of BrC is believed to be more wavelength-dependent, which can be

70 represented by distinct absorption Ångström exponent (AAE) values, i.e., the power exponent

71 of the light absorption coefficient. A typical threshold for the AAE of BC (AAE_{BC}) of 1.6 has

72 been recommended to distinguish BrC from BC (Lack and Cappa, 2010), and the AAE of BrC

73 has been reported as having a wider range (2 to 7) (Hoffer et al., 2005). Based on the difference

74 in the wavelength dependence of light absorption between BC and BrC, previous studies have

75 applied the AAE method to differentiate light absorption by BrC through multiwavelength

76 optical measuring apparatus, such as 3-wavelength Photoacoustic Soot Spectrometer (PASS-3)

77 (Lack and Langridge, 2013), multiwavelength Aethalometer (Olson et al., 2015), etc. Based on

78 the AAE method, the BrC absorption contribution has been estimated to be approximately 6 to

79 41% of total aerosol light absorption at short wavelengths, e.g., at 370 nm and 405 nm

80 (Washenfelder et al., 2015). A uniform AAE_{BC} from ~300 nm up to ~700 nm (Moosmüller et

81 al., 2011) is commonly used when evaluating the BrC absorption contribution using the AAE

82 method. However, it has been reported that the AAE_{BC} can be influenced by the mixing state,

83 BC core size and morphology (Lack and Cappa, 2010). The lensing effect of the coating shell

84 may enhance BC light absorption, the magnitude of which may also depend on wavelength and

85 can alter the value of AAE_{BC} (Liu et al., 2018). Moreover, different values of AAE_{BC} have been

86 found in the near-infrared and UV ranges (Wang et al., 2018). Therefore, using the default value

87 of $AAE_{BC} = 1$ may lead to uncertainty in BrC absorption coefficient estimation.

88 Quantifying BrC optical absorption accurately is essential to interpret aerosol optical depth

89 (AOD), and the corresponding aerosol direct radiative forcing (DRF) on the atmosphere can

90 also be evaluated if the single-scattering albedo (SSA) and extinction coefficient of aerosols are

91 known. The estimation of the DRF of BrC has shown a distinct seasonal variation, indicating

92 the influence of different absorption properties of BrC (Arola et al., 2015). A global simulation

93 study indicated that the average warming effect at the TOA caused by BrC absorption can be

94 up to 0.11 W m^{-2}, corresponding to ~25% of that predicted from BC absorption only (Feng et

95 al., 2013).

96 During the last three decades, rapid economic development has led to severe air pollution

97 problems in the PRD region (Chan and Yao, 2008). With rapid increases in the automobile

98 population and factories, high loadings of SOAs have often been observed (Tan et al., 2016b).

99 Biofuel usage may also play a significant role during wintertime air pollution events in the PRD,

100 indicating that the contribution from BrC light absorption cannot be ignored (Wu et al., 2018).

101 Recently, BrC light absorption has been quantified by Qin et al. (2018) using the AAE method

102 in the PRD region. OA chemical composition was simultaneously measured by a high-

103 resolution time-of-flight aerosol mass spectrometer, and it was found that organic aerosols

104 originating from biomass burning possessed the most intense absorption capability and were

105 largely responsible for BrC absorption. Qin et al. (2018) also suggested that correlations

106 between OA chemical compositions and BrC absorption were wavelength-dependent.

107 In this paper, we applied the homologous AAE differentiation method to quantify the fraction

108 of aerosol light absorption by BrC using the measurements from a seven-wavelength

109 Aethalometer. The potential error incurred with this methodology was determined using Mie

110 theory simulations, especially for various complex refractive indexes of the BC core and the

111 coating material. The correlation between BrC light absorption and water-soluble ions, which

112 is used as the source tracer, was employed to identify potential BrC sources. An atmospheric

113 radiative transfer model has also been applied to evaluate the impact of BrC on direct radiative

114 forcing using surface-based aerosol optical properties and satellite-based surface-albedo data.

115 The magnitudes of aerosol radiative forcing at the top of the atmosphere due to BC and BrC

116 were also individually quantified.

117 **2 Methodology**

118 **2.1 Sampling site**

119 Field observations were conducted at the Panyu station (113°21´E, 23°00´N), which is a

120 monitoring site of the Chinese Meteorological Administration (CMA) Atmospheric Watch

121 Network (CAWNET) that is located on the summit of Dazhengang Mountain (approximately

122 150 m above sea level) in Guangzhou, China. Fig. 1 shows the location of the Panyu site, which

123 is situated at the center of the PRD and is separated from residential areas by at least 500 m.

124 Some agricultural fields can be found to the west of the site. Although there were no significant

125 pollution sources nearby, this suburban site was strongly affected by pollutants transported from

126 the urban area of Guangzhou and crop residual fires transported from the rural area of the PRD.

127 The field campaign was conducted from 29 November 2014 to 2 January 2015. During the

128 measurement period, aerosol light scattering and extinction, BC concentration, particle number

129 size distribution (PNSD), OC concentration, and the water-soluble ion concentrations of $PM_{2.5}$

130 were continuously monitored.

131 **2.2 Measurements and data analysis**

132 All instruments were housed inside the 2nd floor measurement room of a ~5-m tall, 2-story

133 building. The ambient sample was taken on the roof by a 2-m long, 12.7-mm OD stainless steel

134 inlet, and a $PM_{2.5}$ cyclone sampler was also used. The metal tubing was thermally insulated and

135   maintained at a constant temperature of ~25°C. A diffusion drier was also used in-line to dry

136   the relative humidity (RH) of the air sample below 30% before further analysis.

137   **2.2.1 Measurements of relevant species**

138   A TSI-3936 scanning mobility particle sizer (SMPS) and a TSI-3321 aerodynamic particle sizer

139   (APS) were utilized to measure the 10 to 500 nm mobility diameter and 0.5 to 2.5 μm

140   aerodynamic diameter of the PNSD, respectively. The aerodynamic diameters of the APS data

141   were converted into mobility diameters using a material density of 1.7 g cm^{-3}. A detailed data

142   merging method has been described by Cheng et al. (2006). Furthermore, the pipe diffusion

143   loss of SMPS has been corrected using the empirical formula proposed by Kulkarni et al. (1996).

144   An AE-33 Aethalometer (Magee Scientific Inc.) was utilized for BC mass concentration

145   measurement, which was derived from optical attenuation using a mass absorption cross section

146   (MAC) of 7.77 m^2 g^{-1} at 880 nm. The sensitivity of AE-33 was approximately 0.03 μg m^{-3} for

147   a 1-min time resolution and a 5.0 liter per minute (LPM) sample flow rate.

148   The PM$_{2.5}$ mass concentration was measured by an Environment Dust Monitor (Model

149   EDM180, GRIMM Inc.), which monitored the mass concentration of PM$_{2.5}$ and PM$_{10}$

150   simultaneously.

151   Water-soluble ions (potassium (K$^+$), calcium (Ca^{2+}), magnesium (Mg^{2+}), chloride (Cl$^-$), sulfate

152   (SO$_4^{2-}$), nitrate (NO$_3^-$), and ammonium (NH$_4^+$)) were measured with the Monitor for AeRosols

153   and Gases in Air (MARGA) (Model ADI2080, Metrohm Inc.), which is an online analyzer for

154   semi-continuous measurements of gases and water-soluble ions in aerosols (Li et al., 2010).

155   The MARGA was automatically calibrated with standard internal solutions during field

156   measurement. The MARGA utilized its own PM$_{2.5}$ sampling system provided by the

157   manufacturer.

158   The OC mass concentration was measured by a Sunset online OC/EC analyzer (Model RT-4)

159   with a laser transmittance-based charring correction (Wu et al., 2018). The sample flow rate of

160   the OC/EC analyzer was maintained at 8 LPM. For each measurement cycle (one hour),

161   samples were collected onto a quartz filter within the first 45 min and then thermal-optically

162   analyzed during the remaining 15 min. First, OC was completely volatized in oxygen-free

163   helium with a stepwise ramped temperature (600 °C and 840 °C). In the second stage, the

164   temperature was reduced to 550 °C, and then EC and pyrolyzed carbon (PC) were combusted

165   in an oxidizing atmosphere (10% oxygen in helium), while the temperature was increased up

166   to 870 °C step by step. The CO_2 converted from all of the carbon components was then

167   quantified by a nondispersive infrared absorption CO_2 sensor (Lin et al., 2009). An internal

168   calibration peak made by 5% methane in helium was applied to quantify OC and EC. To correct

169   the PC converted from OC to EC, a tunable pulsed diode laser beam was used to monitor the

170   laser transmittance through the quartz filter throughout the thermal-optical analysis (Bauer et

171   al., 2012).

172   **2.2.2 Measurements of optical properties**

173   Light extinction by aerosols at 532 nm was detected using a cavity ring-down aerosol extinction

174   spectrometer (CRDS) (Model XG-1000, Hexin Inc.) by measuring the decay times of laser

175   intensity through the aerosol-containing sample and the filtered background air sample under

176   the same conditions. The extinction coefficient (σ_{ext}) was calculated using the procedure

177   described by Khalizov et al. (2009).

178   Aerosol total scattering (σ_{sp}) was measured by a TSI-3563 integrated nephelometer at three

179   wavelengths (i.e., 450 nm, 550 nm, and 700 nm) and was calibrated with CO_2 following the

180   manual instructions. Particle free air was used to check the nephelometer background signal

181   once every two hours. The scattering coefficients at other wavelengths were extrapolated using

182   the following equations:

$$SAE = -\frac{ln\left(\sigma_{scat,\lambda_0}\right) - ln\left(\sigma_{scat,550nm}\right)}{ln(\lambda_0) - ln(550)} \tag{1}$$

183

$$\sigma_{scat}(\lambda) = \sigma_{scat}(550) \cdot \left(\frac{\lambda}{550}\right)^{-SAE} \tag{2}$$

184

185   where λ_0=450 nm is for wavelengths less than 550 nm and λ_0=700 nm is for wavelengths greater

186   than 550 nm. The corresponding time series of extinction coefficients, scattering coefficients,

187   and SSA at 532 nm was displayed in Fig. S1.

188   The Aethalometer is also used for multi-wavelength light absorption measurements in this study.

189   The seven-wavelength aerosol light attenuation coefficients (σ_{ATN}) were converted into aerosol

190   light absorption coefficients (σ_{abs}) using Eq. (3) (Coen et al., 2010), where k is the parameter

191   that accounts for the loading effect, ATN is the light attenuation through the filter with sample

192   loading and C_{ref} is a fixed multiple scattering parameter.

$$\sigma_{abs} = \frac{\sigma_{ATN}}{(1 - k \cdot ATN) \cdot C_{ref}} \tag{3}$$

193

194 The real-time k value was retrieved using the dual-spot loading correction algorithm developed

195 by Drinovec et al. (2015). The detailed formula of ATN can also be found in Drinovec et al.

196 (2015). C_{ref} is considered a constant that strongly depends on the filter matrix effect. However,

197 some studies have suggested that C_{ref} may vary with wavelength (Arnott et al., 2005;Segura et al.,

198 2014). For internal combustion engines and biomass burning, C_{ref} at 370 nm was expected to be

199 approximately 12% and 18% less than C_{ref} at 532 nm for the aerosol component, respectively

200 (Schmid et al., 2006). Different ambient observations also showed that C_{ref} may have regional

201 specificity, even though it was retrieved by the same methodology (Coen et al., 2010). In this

202 study, C_{ref} =3.29 was used in Eq. (3) at each wavelength, and this value was derived from the

203 slope of σ_{ATN} measured by the Aethalometer vs. σ_{abs}, which was deduced from the CRDS and

204 nephelometer measurements. This C_{ref} was also very similar to the C_{ref} of 3.48 determined from

205 an inter-comparison study between an Aethalometer and a photoacoustic soot spectrometer

206 during a field campaign conducted in the PRD region in 2004 (Wu et al., 2009).

207 The BC light absorption at certain wavelengths was derived from the absorption coefficient σ_{abs}

208 according to Beer-Lambert's law, and its variation between different pairs of wavelengths (i.e.,

209 $\sigma_{abs,BC,\lambda}$) is denoted by the absorption Ångström exponent (AAE) equation developed by

210 Ångström (1929):

$$211 \qquad \sigma_{abs,BC,\lambda} = \sigma_{abs,BC,\lambda_0} \times (\lambda_0 / \lambda)^{-AAE_{BC}} \qquad (4)$$

212 It has been suggested that the AAE of BC may vary between short and long wavelength ranges

213 (Lack and Cappa, 2010); hence, applying a wavelength-independent AAE_{BC} may lead to

214 uncertainties in the BC absorption calculation from one wavelength to another. In this work,

215 the light absorptions of BC at various wavelengths were retrieved by a modified wavelength-

216 dependent AAE differentiation method conducted by Wang et al. (2018):

$$217 \qquad \sigma_{abs,BC,\lambda_1} = \sigma_{abs,BC,,880nm} \times (\frac{880}{\lambda_1})^{AAE_{BC,520-880nm}} \qquad (5.1)$$

$$218 \qquad \sigma_{abs,BC,\lambda_2} = \sigma_{abs,BC,880nm} \times (\frac{880}{520})^{AAE_{BC,520-880nm}} \times (\frac{520}{\lambda_2})^{AAE_{BC,370-520nm}} \qquad (5.2)$$

219 Here, $\sigma_{abs,BC,\lambda_1}$ represents the absorption coefficient due to only BC greater than 520 nm, and

220 $\sigma_{abs,BC,\lambda_2}$ represents the absorption coefficient of BC less than 520 nm. $AAE_{BC, \lambda_i - \lambda_{i+1}}$ (i=1, 2

221 and 3) represents the AAE of BC between a longer and shorter wavelength at λ_i=880, 520 and

222 370 nm and was calculated as:

$$AAE_{BC,\lambda_i-\lambda_{i+1}} = -\frac{ln(\sigma_{abs,BC,\lambda_i}) - ln(\sigma_{abs,BC,\lambda_{i+1}})}{ln(\lambda_i) - ln(\lambda_{i+1})} \qquad (6)$$

Accordingly, BrC absorption at a certain wavelength λ ($\sigma_{abs,BrC,\lambda}$) was equal to the value of total aerosol absorption ($\sigma_{abs,\lambda}$) minus BC absorption ($\sigma_{abs,BC,\lambda}$):

$$\sigma_{abs,BrC,\lambda} = \sigma_{abs,\lambda} - \sigma_{abs,BC,\lambda} \qquad (7)$$

The light absorption data at 880 nm ($\sigma_{abs,880nm}$) were selected to represent BC absorption ($\sigma_{abs,BC,880nm}$), which shall not be affected by BrC (Drinovec et al., 2015). It has been reported that the dust-related contributions of PM$_{2.5}$ were normally less than 5% in wintertime in Guangzhou; therefore, the influence from dust could be negligible in this study (Huang et al., 2014).

2.2.3 Estimation of AAE$_{BC}$

Traditionally, AAE$_{BC}$ was believed to be close to 1.0 (Bodhaine, 1995), which has been commonly used for BC measurements (Olson et al., 2015). However, studies have demonstrated that AAE$_{BC}$ can be affected by the refractive index of coating materials, mixing state, morphology, and BC core size (Liu et al., 2015). Therefore, using the default AAE$_{BC}$ = 1 may lead to uncertainty in BrC absorption estimation. To obtain the correct AAE$_{BC}$, a series of Mie theory calculations were conducted using a simplified core-shell model (Bohren and Huffman, 1983;Wang et al., 2018). We used a modified BHCOAT code and BHMIE code to calculate the aerosol optical properties of the core-shell and external mixture at different wavelengths (Cheng et al., 2006). In the Mie theory, a particle is taken as a perfect homogeneous sphere, and its extinction and scattering efficiencies, $Q_{ext,Mie,\lambda}$ and $Q_{scat,Mie,\lambda}$, respectively, are expressed as (Mie, 1908;Seinfeld and Pandis, 1998):

$$Q_{ext,Mie,\lambda} = \frac{2}{\alpha^2}\sum_{n=1}^{\infty}[(2n+1)Re(a_n+b_n)] \qquad (8)$$

$$Q_{scat,Mie,\lambda} = \frac{2}{\alpha^2}\sum_{n=1}^{\infty}[(2n+1)(|a_n|^2+|b_n|^2)] \qquad (9)$$

where $\alpha = \pi D_p/\lambda$ is the size parameter; a_n and b_n are functions of the complex refractive index (RI) and α in the Riccati-Bessel form, respectively. *Re* in Eq. (8) denotes that only the real part of RI is taken. The absorption efficiency ($Q_{abs,Mie,\lambda}$) is thus the difference between the extinction and scattering efficiencies:

$$Q_{abs,Mie,\lambda} = Q_{ext,Mie,\lambda} - Q_{scat,Mie,\lambda} \tag{10}$$

Then, the absorption coefficient $\sigma_{abs,Mie,\lambda}$ was obtained by the following (Bricaud and Morel, 1986):

$$\sigma_{abs,Mie,\lambda} = \int Q_{abs,Mie,\lambda} \cdot (\frac{\pi}{4}D_p^2) \cdot N(\log D_p) \cdot d\log D_p \tag{11}$$

where $N(\log D_p)$ is the PNSD function. A two-component parameterization of dry particles, i.e., the BC core and the nonlight-absorbing species, was applied to calculate aerosol optical properties here (Wex et al., 2002). $\widetilde{m}_{core}$ represents the RI of the BC core, and $\widetilde{m}_{non}$ represents the RI of nonlight-absorbing particles.

In a realistic atmosphere, some nonlight-absorbing particles may exist independently without BC (Liu et al., 2013; Cheung et al., 2016). In this work, the portion of nonlight-absorbing particles at a certain size (D_p) was determined by our previous measurements at the same site using a Volatility Tandem Differential Mobility Analyzer (V-TDMA), during which completely vaporized (CV) particles at 300°C were referred to as nonlight-absorbing particles that externally mixed with other BC-containing particles. Thus, the PNSD of CV particles ($N(logD_p)_{CV}$) and BC-containing particles ($N(logD_p)_{BC}$) can be given by the following equations:

$$N(logD_p)_{CV} = N(logD_p)_{measure} \cdot \Phi(D_p)_{N,CV} \tag{12}$$

$$N(logD_p)_{BC} = N(logD_p)_{measure} \cdot (1 - \Phi(D_p)_{N,CV}) \tag{13}$$

where $N(logD_p)_{measure}$ is the PNSD of the measured particles from SMPS and APS. $\Phi(D_p)_{N,CV}$ was the number fraction of CV particles in different size bin.

A previous study applied three kinds of BC mixture models to calculate the aerosol optical properties, including external, homogenously internal and core-shell mixtures (Bohren and Huffman, 2007;Seinfeld and Pandis, 1998). To quantify the mixing state of BC, r_{ext} was defined as the mass fraction of externally mixed BC (M_{ext}) in total BC (M_{BC}):

$$r_{ext} = \frac{M_{ext}}{M_{BC}} \tag{14}$$

Tan et al. (2016) suggested that two extreme conditions of external and core-shell mixtures comprised the actual mixing state of BC in the PRD. Hence, we simply divided the PNSD of BC into the PNSD from an external mixture of BC and a core-shell mixture of BC. The PNSDs

278   of externally mixed BC particles and core-shell mixed BC particles were referred to by the

279   following equations with a given r_{ext}.

$$N(logD_p)_{ext} = N(logD_p)_{BC} \cdot f_{BC} \cdot r_{ext} \tag{15}$$

$$N(logD_p)_{core-shell} = N(logD_p)_{BC} \cdot (1 - f_{BC} \cdot r_{ext}) \tag{16}$$

282   f_{BC} was defined as the BC volume fraction in the BC-containing particle volume, which can be

283   converted from the BC mass concentration:

$$f_{BC} = \frac{M_{BC}}{\rho_{BC} \cdot \Sigma_{D_P} N(logD_p)_{BC} \cdot (\frac{\pi}{6} \cdot D_p^3)} \tag{17}$$

285   where ρ_{BC} is the density of BC and is assumed to be 1.5 g cm^{-3} (Ma et al., 2012); M_{BC} is the BC

286   mass concentration derived from the multi-angle absorption photometer (MAAP), which was

287   obtained by an empirical formula from the Aethalometer that measured the BC concentration

288   ($M_{BC,AE}$), as proposed by Wu et al. (2009):

$$M_{BC} = 0.897 \cdot M_{BC, AE} - 0.062 \tag{18}$$

290   The PNSDs of externally mixed nonlight-absorbing particles and externally mixed BC particles

291   were input into the BHMIE code, and the PNSD of the core-shell mixed particles was imported

292   into the BHCOAT code. Another critical parameter for the core-shell model was the diameter

293   of the BC core. For the simplified core-shell model we applied, the visualization was that a

294   homogeneous BC core sphere was encapsulated in a shell of non-absorbing coating (Bohren

295   and Huffman, 2007). Without size-resolved coating thickness measurements, core-shell mixed

296   particles simply assumed that cores with the same diameter had the same coating thickness.

297   Therefore, the diameter of the BC core was calculated as follows:

$$D_{core} = D_p \cdot (\frac{f_{BC} - f_{BC} \cdot r_{ext}}{1 - f_{BC} \cdot r_{ext}})^{\frac{1}{3}} \tag{19}$$

299   D_{core} and D_p are inputted as parameters into a_n and b_n, respectively, which was described by

300   Bohren and Huffman (2007). The corresponding time series of size distribution of the derived

301   external BC and internal BC core were illustrated in Fig. S2. Thus, the $\sigma_{abs,BC,Mie, \lambda_i}$ values of

302   all six wavelengths were calculated through the Mie model, and then the AAE$_{BC}$ values of those

303   five wavelengths were obtained using Eq. (6). The performance of this empirically determined

304   calculation method has been compared with other possible BC mixing schemes in details (see

305   Table 1).

306   **2.2.4 Atmospheric radiative transfer model**

307 In this work, theSanta Barbara DISORT Atmospheric Radiative Transfer (SBDART) model

308 was employed to estimate the DRF of BrC absorption, i.e., its effects on the downward and

309 upward fluxes (F in W m^{-2}) of solar radiation at the TOA. SBDART is a software tool that can

310 be used to compute plane-parallel radiative transfer under both clear and cloudy conditions

311 within the atmosphere. More details about this model have been described by Ricchiazzi et al.

312 (1998). Both ground measurements and remote sensing data were used in the simulation. The

313 surface albedo was derived from a 500 m resolution MODIS BRDF/albedo model parameter

314 product (MCD43A3, daily). The MCD43A3 products are the total shortwave broadband black-

315 sky albedo (α_{BSA}) and white-sky albedo (α_{WSA}), while the actual surface albedo (α) was

316 computed from a linear combination of α_{WSA} and α_{BSA}, which were weighted by the diffuse ratio

317 (r_d) and direct ratio ($1-r_d$), respectively:

$$\alpha=(1 - r_d) \cdot \alpha_{BSA}+r_d \cdot \alpha_{WSA} \tag{20}$$

319 r_d was obtained from an exponential fit of Eq. (21) based on empirical observations (Stokes and

320 Schwartz, 1994;Roesch, 2004):

$$r_d=0.122+0.85e^{-4.8\mu_0} \tag{21}$$

322 where μ_0 is the cosine of the zenith angle, which is calculated by the model for any specified

323 date, time, and latitude and longitude of the site. The surface-based aerosol optical properties,

324 including the aerosol light absorption coefficients of both BC and BrC, i.e., differentiated from

325 each other under the assumption of uniform AAE$_{BC}$, along with the nephelometer-measured

326 aerosol scattering coefficients, were used to calculate the SSA at different wavelengths

327 according to Eq. (22),

$$SSA(\lambda)=\frac{\sigma_{scat,\,\lambda}}{\sigma_{abs,\,BrC,\lambda}+\sigma_{abs,\,BC,\lambda}+\sigma_{scat,\lambda}} \tag{22}$$

329 which was then used in the model calculation. Finally, the AOD and asymmetry factor (ASY)

330 at 440, 675 and 870 nm were derived from the Aerosol Robotic Network (AERONET)

331 measurements at the Hong Kong Polytechnic University site (Holben et al., 1998), which is

332 approximately 115 km to the southeast of the Panyu site. The tropical atmospheric profile was

333 used in the SBDART model based on the prevailing weather conditions in the PRD. The aerosol

334 DRF (ΔF) was calculated as the difference between the downward and upward radiation fluxes:

$$\Delta F = F \downarrow - F \uparrow \tag{23}$$

3 Results and discussion

3.1 Aerosol light absorption

The AAE_{BC} is widely defined as the uniform representation of the wavelength dependence of a BC particle (Olson et al., 2015). In reality, AAE_{BC} may vary significantly with BC containing aerosols of different sizes, mixing states, and morphologies (Scarnato et al., 2013;Lack and Langridge, 2013). In fact, some studies showed that the AAE of a large-size, pure BC core may be less than 1.0 (Liu et al., 2018) and that the AAE of BC coated with a non-absorbing shell may be larger than that under uniformity (Lack and Cappa, 2010).

It has been suggested that a significant fraction of smaller size particles is non BC-containing (Ma et al., 2017;Cheung et al., 2016). BC and non-BC materials can also be externally or internally mixed. Although size resolved BC measurements were not available during this work, we have conducted size resolved Volatility Tandem Differential Mobility Analyzer (V-TDMA) measurements at 300℃ for 40, 80, 110, 150, 200 and 300 nm, respectively, during an earlier field campaign (February 2014) at the same site as in this work. At 300℃, all non-BC particle will be completely vaporized (CV) and thus the portion of non BC particles at such size, denoted as $\Phi_{N,CV}$, can be determined. The average $\Phi_{N,CV}$ values were 0.384, 0.181, 0.180, 0.158, 0.143 and 0.137, corresponding to 40, 80, 110, 150, 200 and 300 nm (see Fig. S3), respectively (Cheung et al., 2016;Tan et al., 2016a). The size-independent $\Phi_{N,CV}$ was interpolated linearly with these six diameters. For particle size larger than 300 nm and less than 40 nm, $\Phi_{N,CV}$ values were set to 0.137 and 0.384, respectively. For particle size larger than 300 nm and less than 40 nm, $\Phi_{N,CV}$ values were set to 0.137 and 0.384, respectively. Accordingly, the complete distribution of $\Phi_{N,CV}$ for the whole PNSD was obtained. The mixing states of BC particles were also estimated here, i.e., the mass portion of externally mixed BC with respect to total BC, denoted as r_{ext}. The value of r_{ext} was taken as 0.58, which was obtained using an optical closure method during a previous field experiment at this site (Tan et al., 2016a). During the following Mie theory calculation, a fixed refractive index ($\widetilde{m}_{core}$=1.80-0.54i, $\widetilde{m}_{non}$=1.55-10^{-7}i) was adopted for the whole size range. Accordingly, the calculated BC absorption at 880 nm (Abs_{880}) was 21.869 Mm^{-1}, which is reasonably close to the measured mean value of 21.199 Mm^{-1}. To further validate our calculation scheme (Base Case), we have considered several extreme cases. Case 1: BC is completely externally mixed with non-BC particles, i.e., $\Phi_{N,CV} = 0$ and $r_{ext} = 1$;

366   Case 2: BC is present in every size bin and BC is completely internally mixed with non-BC

367   material, i.e., $\Phi_{N,CV} = 0$ and $r_{ext} = 0$; Case 3: BC is both internally and externally mixed but there

368   is no non BC-containing particles, i.e., $\Phi_{N,CV} = 0$ and $r_{ext} = 0.58$; Case 4: BC is internally mixed

369   with non-BC material and there is non-BC particles present, i.e., $\Phi_{N,CV}$ ranges from 0.384 to

370   0.137 and $r_{ext} = 0$; Case 5: the same as case 4 except assuming a fixed non-BC to BC ratio of

371   0.5, i.e., $\Phi_{N,CV} = 0.5$, $r_{ext} = 0$; Case 6: the same as case 5 except that some externally mixed BC

372   is also present, i.e., $\Phi_{N,CV} = 0.5$, $r_{ext} = 0.58$. The calculation results are listed in Table 1. Evidently,

373   case 1 (complete externally mixed) will significantly underestimate the measured Abs_{880},

374   indicating that most BC particles were not likely externally mixed at the Panyu site. Complete

375   internal mixing state (case 2, 4, and 5), on the contrary, would substantially overestimate the

376   BC absorption regardless the form of BC core distribution function. However, when the r_{ext}

377   were considered (case base, 3, and 6), the calculated Abs_{880} values were all very close to the

378   measured value.

379   When the AAE_{BC} was assumed to be uniform, the campaign-averaged σ_{BrC} values were

380   17.6±13.7 Mm^{-1} at 370 nm, 9.7±7.9 Mm^{-1} at 470 nm, 5.8±5.1 Mm^{-1} at 520 nm, 4.0±3.5 Mm^{-1} at

381   590 nm and 2.3±2.1 Mm^{-1} at 660 nm. At the corresponding wavelengths, BrC absorption

382   contributed 26.2±8.5%, 20.0±7.3%, 14.3±6.5%, 11.7±5.3%, and 7.8±4.1% to the total aerosol

383   absorption, respectively. When the AAE_{BC} was applied as the result of the Mie model

384   calculation, the corrected campaign-averaged $\sigma_{abs,BrC}$ values were 23.5±17.7 Mm^{-1} at 370 nm,

385   11.8±9.5 Mm^{-1} at 470 nm, 6.7±5.7 Mm^{-1} at 520 nm, 4.6±3.9 Mm^{-1} at 590 nm and 2.6±2.3 Mm^{-}

386   ^{1} at 660 nm. At the corresponding wavelengths, BrC absorption contributed 34.1±8.0%,

387   23.7±7.3%, 16.0±6.7%, 13.0±5.4%, and 8.7±4.3% to the total aerosol absorption (see Fig. 2),

388   respectively. Evidently, aerosol light absorption was predominantly due to BC; however, BrC

389   also played a significant role, especially at shorter wavelengths. Table 2 shows the

390   intercomparison of BrC light absorption in the near UV range between this work and other

391   studies in the East Asian region. Clearly, the reported values vary substantially, and our result

392   is toward the lower end of values. Figure S4 displayed the time series of particle AAE measured

393   by the Aethalometer and AAE_{BC} was derived from Mie model calculation. The AAE_{BC} was

394   almost always lower than AAE, indicating appreciable BrC light absorption at the Panyu site.

395   **3.2 Uncertainty in BC and BrC optical differentiation**

396   Theoretically, the magnitude of BC absorptions can be affected by both parts of the complex

397   refractive indexes (RIs); thus, AAE_{BC} may also vary with the RIs of both the BC core and

398   coating shell. In fact, RI was also one of the least known properties of BC and other coating

399   materials with negligible absorbing capabilities. The refractive index of the BC core ($\widetilde{m}_{core}$)

400   displays a wide range of variations (Liu et al., 2018). Typically, the real and imaginary parts of

401   the RI can vary from 1.5 to 2.0 and 0.5 to 1.1, respectively. In addition, the shell was assumed

402   to consist of non-absorbing material in the core-shell model, i.e., its imaginary RI was set to be

403   close to zero (10^{-7}). The real part of the non-absorbing material RI ($\widetilde{m}_{non}$) may vary from 1.35

404   to 1.6 due to the presence of OA (Zhang et al., 2018;Redmond and Thompson, 2011) and

405   inorganic salts (Erlick et al., 2011). Hence, it is necessary to investigate the uncertainties

406   associated with the variations in AAE_{BC} by varying the RIs of both the BC core and the non-

407   absorbing materials.

408   Figure 3 shows the impacts of RI on the evaluations of AAE_{BC} based on core-shell and external

409   configuration, where the RI of the BC core was set to be constant, i.e., $\widetilde{m}_{core}$=1.80-0.54i, and

410   the real part of $\widetilde{m}_{non}$ varied from 1.35 to 1.6 at an interval of 0.05, with the imaginary part of

411      $\widetilde{m}_{non}$ set at 10^{-7}. As shown in Fig. 3a, the calculated AAE_{BC} for the core-shell model was higher

412   than 1.0 at longer wavelengths (520 to 880 nm) and lower than 1.0 at shorter wavelengths (370

413   to 520 nm) (the red line in Fig. 3 denotes AAE_{BC}=1). The averaged $AAE_{BC,370-520nm}$ ranged from

414   0.84 to 0.87, and the $AAE_{BC,520-880nm}$ ranged from 1.07 to 1.15, indicating that the $AAE_{BC,520-880nm}$

415   appeared to be more sensitive to the shell's real part than $AAE_{BC,370-520nm}$. Even if the shell

416   material was assumed to be non-absorbing, the variation in the real RI of the shell, which was

417   referred to as the real part of $\widetilde{m}_{non}$, still led to changes in the shell's refractivity and

418   correspondingly altered its lensing effect, causing a change in AAE_{BC}. Meanwhile, $AAE_{BC,370-520nm}$

419   and $AAE_{BC,520-880nm}$ generally increased with an increasing real part of the shell. In Fig. 3b,

420   under the externally mixed conditions, $AAE_{BC,370-520nm}$ and $AAE_{BC,520-880nm}$ were both less than

421   1.0. The average $AAE_{BC,370-520nm}$ was 0.33, and the average $AAE_{BC,520-880nm}$ was 0.63. These

422   values were far less than the values under core-shell mixture conditions. In the external mixture

423   model, the BC core and nonlight-absorbing materials were assumed to exist dependently, and

424   then the optical properties of these two components were considered separately. Therefore,

425   altering the real part of the externally mixed non-absorbing material would not affect the light

426   absorption property of the BC core or AAE_{BC}.

427   The impacts of the BC core on AAE_{BC} are shown in Fig. 4, where the refractive index of

428   nonlight-absorbing materials was assumed to be $\widetilde{m}_{non}=1.55\text{-}10^{-7}i$ and $\widetilde{m}_{non}$ was wavelength-

429   independent. Fig. 4 was obtained with a core-shell mixture model (Fig. 4a and 4b) and an

430   external mixture model (Fig. 4c and 4d) by varying the real part of $\widetilde{m}_{core}$ from 1.5 to 2.0 with

431   a step of 0.05 and varying the imaginary part of the $\widetilde{m}_{core}$ from 0.4 to 1.0 with a step of 0.05,

432   respectively. As shown in Figs. 4a and 4b, for the core-shell mixture, the averaged $AAE_{BC,370\text{-}}$

433      $_{520nm}$ ranged from 0.55 to 0.99, and the averaged $AAE_{BC,520\text{-}880nm}$ ranged from 0.84 to 1.27. The

434   AAE_{BC} at a certain wavelength generally increased when increasing the real part of $\widetilde{m}_{core}$ but

435   decreased when increasing the imaginary part of $\widetilde{m}_{core}$. The AAE_{BC} appeared to be more

436   sensitive to the imaginary part of $\widetilde{m}_{core}$ than the real part of $\widetilde{m}_{core}$ because the imaginary part

437   of $\widetilde{m}_{core}$ was directly related to the light-absorbing properties of particles. In Fig. 4c and 4d,

438   for the external mixture, the averaged $AAE_{BC,370\text{-}520nm}$ ranged from 0.04 to 0.45 and the averaged

439      $AAE_{BC,520\text{-}880nm}$ ranged from 0.28 to 0.79, while the averaged $AAE_{BC,370\text{-}520nm}$ and $AAE_{BC,520\text{-}}$

440      $_{880nm}$ were both less than 1.0. Similar to the core-shell mixture, the $AAE_{BC,520\text{-}880nm}$ increased

441   when increasing the real part of $\widetilde{m}_{core}$ but decreased when increasing the imaginary part of

442      $\widetilde{m}_{core}$. However, the variation patterns of $AAE_{BC,370\text{-}520nm}$ were different from those of $AAE_{BC,520\text{-}}$

443      $_{880nm}$. The $AAE_{BC,370\text{-}520nm}$ values were not changed by altering the real part of $\widetilde{m}_{core}$ within the

444   low imaginary part of $\widetilde{m}_{core}$, whereas the $AAE_{BC,370\text{-}520nm}$ values still increased when increasing

445   the real part of $\widetilde{m}_{core}$ within the high imaginary part of $\widetilde{m}_{core}$. A possible explanation was that

446   the externally mixed BC core had weak light absorption within the low imaginary part of $\widetilde{m}_{core}$,

447   causing the $AAE_{BC,370\text{-}520nm}$ values to be insensitive to the real part of $\widetilde{m}_{core}$. The $AAE_{BC,520\text{-}880nm}$

448   values were higher than the $AAE_{BC,370\text{-}520nm}$ values regardless of whether in they were for the

449   core-shell mixture or external mixture. In addition, the AAE_{BC} values conducted by the core-

450   shell mixture were higher than those conducted by the external mixture.

451   Figure 4 demonstrates that the variation in the imaginary RI of the BC core has the most

452   significant impact on the estimated AAE_{BC}, indicating that the chemical component of BC

453   emitted from different sources leads to a large uncertainty in AAE_{BC} estimation. At the same

454   time, the influence arising from varying the real RI of the BC core was relatively moderate.

455   Nevertheless, Fig. 3 demonstrated that change in the real RI of the non-absorbing materials

456 caused the least/no impact compared to that caused by the variations in the complex RI of the

457 BC core.

458 It should be pointed out that most BC-containing particles are often observed as fractal rather

459 than spherical in shape (Katrinak et al., 1993). Because the Mie model assumes that all particles

460 are spherical, it may lead to potential uncertainty for the estimation of AAE_{BC} and BrC

461 absorption contributions. Moreover, the externally mixed soot aggregates were "chain-like" or

462 "puff-like" in the PRD dry season (Feng et al., 2010), in which the fractal dimension (D_f) was

463 between 1.5 and 2.0. Coating soot aggregates were likely sphere (D_f approaches 3) from the

464 high-resolution transmission electron microscopy (TEM) measurements taken in Hongkong

465 ((Zhou et al., 2014)). A soot aggregate sensitivity study with the superposition T-matrix method

466 indicated that using the assumption of volume-equivalent spheres for the soot aggregates may

467 result in an overestimation of approximately up to 15% and an underestimation of

468 approximately up to 50% in the predicted 870 nm light absorption when the D_f is between 1.5

469 and 3.0 (Liu et al., 2008). However, it should be recognized that the complex shapes or positions

470 of the BC core inside the particle make it impractical to be numerically simulated in the exact

471 details. By far the Mie model with a core-shell configuration would be the most practical and

472 effective simulation scheme for BC particle optical property simulation.

473 Furthermore, we have performed Monte Carlo simulations to evaluate the uncertainties of the

474 Mie calculation performed during this work. In the simulation, a sequence of random numbers

475 or errors were applied to the input parameters, and then the corresponding uncertainties of

476 particle light absorption and AAE_{BC} by were computed using the Mie model. Five hundred of

477 reiteration were conducted during the simulation such that the random errors will be normally

478 distributed. The standard deviations (σ) of all input parameters are listed in Table S1. In order

479 to cover the effect of extreme value, we used a range of $\pm 3\sigma$, or a confidence level of 99%, in

480 the Mont Carlo simulation. Table S2 listed the Monte Carlo simulation results, i.e., the average

481 relative standard deviations (σ_{Mie}) of the calculated BC light absorption at 880 nm (Abs_{880}),

482 $AAE_{BC,370-520}$, and $AAE_{BC,520-880}$. The uncertainties of the calculated Abs_{880}, $AAE_{BC,370-520}$, and

483 $AAE_{BC,520-880}$ at 2 times of σ_{Mie}, i.e., at a confidence coefficient of 95%, were approximately

484 $\pm 31\%$, $\pm 16\%$, and $\pm 13\%$, respectively. Figure S5a showed the time series of the uncertainties

485 of Abs_{880}, $AAE_{BC,370-520}$ and $AAE_{BC,520-880}$ from Monte Carlo simulation for the campaign period.

486   These uncertainties will certainly be propagated into the calculated BrC absorption

487   contributions, too. Hence, we also estimated the corresponding uncertainties in the BrC

488   absorption contribution results, as shown in Fig. S5b. Accordingly, the averaged lower limits

489   of BrC absorption contributions were 26.8%±9.1% at 370 nm, 17.5%±8.1% at 470 nm,

490   10.1%±7.3% at 520 nm, 8.5%±5.8% at 590 nm and 5.3%±4.5% at 660 nm, respectively, and

491   the averaged upper limits of BrC absorption contribution ratios were 40.7%±7.2% at 370 nm,

492   29.5%±6.7% at 470 nm, 21.1%±6.2% at 520 nm, 17.3%±5.2% at 590 nm and 12.0%±4.1% at

493   660 nm, respectively.

494   **3.3 Characteristics of BrC light absorption, water-soluble ions and OC concentrations**

495   Globally, BrC has been observed to be highly correlated with biomass and biofuel burning

496   emissions (Laskin et al., 2015). Since large quantities of sylvite are present in biomass burning

497   particles, the K^+ abundance has often been used as a biomass burning tracer (Levine, 1991).

498   Figure 5 presents the time series of the OC mass concentration, K^+ concentration, and BrC

499   absorption from 29 November 2014 to 2 January 2015 at the Panyu site. The range of the OC

500   concentration obtained from the OC/EC online analyzer was from 1.5 to 65.2 μg cm$^{-3,}$ and the

501   campaign average was 12.5±7.3 μg cm^{-3}. The BrC absorption hourly mean data were between

502   0.2 and 123.2 Mm$^{-1,}$ and the campaign average was 23.5±17.7 Mm^{-1}. On the other hand, the

503   average K^+ concentration was 1.0 ± 0.7 μg cm^{-3} (ranging from 0 to 5.4 μg cm^{-3}). Clearly, similar

504   trends among OC, K^+, and BrC absorption can be seen during this field campaign (Fig. 5).

505   To investigate the origins of these observed OC, K^+, and BrC, wind rose plots (as shown in Fig.

506   6) were generated for OC, K^+, and BrC absorption, respectively. All three panels of Fig. 6

507   consistently show that the three substances were associated with the same wind pattern. For the

508   entire campaign period, the highest values of OC, K^+, and $\sigma_{abs,BrC,370nm}$ were mostly associated

509   with southwesterly winds with a relatively low wind speed (~2 m s^{-1}). The relatively higher OC

510   and K^+ concentrations were highly related to the seasonal straw burning in the countryside of

511   the PRD located to the west of the Panyu station. In contrast, OC and K^+ concentrations during

512   periods with easterly winds were substantially lower than those during periods with westerly

513   winds. The wind rose plot of $\sigma_{abs,BrC,370nm}$ is shown in Fig. 6c. Similar to OC and K^+, $\sigma_{abs,BrC,370nm}$

514   showed higher values under weak (<2 m s^{-1}) westerly winds and lower values from the north

515   and south, indicating that BrC absorption was likely attributed to local sources and was

516   accumulated under calm wind conditions. Figure S6 showed the 3-day backward trajectory and

517   the fire counts for 5 to 7 (Fig. S6a), 12 to 14 (Fig. S6b) and 24 to 26 (Fig. S6c) in November

518   2014, representing low loading, moderate loading and high loading period. Clearly, the high

519   loading period concurred with stagnant air movement and higher fire counts, indicating the

520   contribution from open fire burning sources. However, there was a detectable difference among

521   the three rose plots of Fig. 6 in the maximum concentration direction. A possible explanation

522   was that although biomass burning emissions were believed to be the dominant and primary

523   source of OC, K^+, and BrC, their emission ratios were highly variable and may change with the

524   type of biofuel and burning condition and may even vary during different stages of burning

525   (Burling et al., 2012). Although biomass burning emissions contain substantial light-absorbing

526   BrC, further atmospheric aging processes may significantly reduce its light-absorbing

527   capability (Satish et al., 2017). Moreover, secondary formation may also lead to BrC formation

528   inside these primary aerosols, such as humic-like substances formed through aqueous-phase

529   reactions, which have been suggested to be an important component of BrC (Andreae and

530   Gelencser, 2006).

531   To further explore the possible sources of BrC optical absorption, the diurnal variations in OC,

532   K^+, $\sigma_{abs,BrC,370nm}$, and $\sigma_{abs,BrC,370nm}$ /OC values are plotted in Fig. 7. The diurnal variation in OC

533   at the Panyu site appeared to be dominated by the development of the planetary boundary layer

534   (PBL) height, i.e., primary emissions accumulated at night and were swiftly diluted by vertical

535   mixing in the morning. The slight increase in OC in the afternoon indicated that photochemistry

536   may have still weakly contributed to SOA formation. Fig. 7b shows the diurnal variation in K^+.

537   Unlike OC, K^+ shows a small peak at approximately 6 AM, which was consistent with breakfast

538   time and was very likely due to cooking activities using biofuel. No lunch and dinner time K^+

539   peaks were observed. The most likely explanation is that the boundary layer height is much

540   higher during lunch and dinner time than in the early morning, providing a much better

541   atmospheric diffusion condition for air pollutants. It is still a common practice to collect straw

542   as biofuel in local rural areas, which can be visually spotted but is not heavily utilized in the

543   region. However, the diurnal profile of $\sigma_{abs,BrC,370nm}$ (see Fig. 7c) shows the combined features

544   of OC and K^+ since both primary and secondary processes affect its intensity. The nighttime

545   increasing trend was most likely attributed to straw burning activities in early winter in nearby

546   rural areas that continued to accumulate within the shallow PBL (Jiang et al., 2013).

547     $\sigma_{abs,BrC,370nm}$/OC, i.e., the mass absorption coefficient of BrC (MAC$_{BrC}$) (Fig. 7d), showed a

548   relatively flat pattern, with a pronounced dip in the afternoon and higher values at nighttime,

549   which was likely due to enhanced primary emissions and stable stratification at nighttime.

550   Declining trends during the late morning and afternoon hours indicated that the aging process

551   and photochemical production may reduce the light-absorbing capacity of BrC (Qin et al.,

552   2018).

553   Furthermore, Fig. 8 shows the linear regression analysis results used to evaluate the correlations

554   of $\sigma_{abs,BrC,370nm}$ with the OC, K$^+$, Ca^{2+}, Mg^{2+}, Cl$^-$, SO$_4^{2-}$, NO$_3^-$, and NH$_4^+$ concentrations. The best

555   correlations can be found between $\sigma_{abs,BrC,370nm}$ and K$^+$ (R^2=0.6148), followed by those between

556     $\sigma_{abs,BrC,370nm}$ and OC (R^2=0.4514), NO$_3^-$ (R^2=0.4224) and NH$_4^+$ (R^2=0.4656). Source

557   apportionment analysis of OA and BrC absorption in Beijing and Guangzhou illustrated that

558   biomass burning organic aerosols (BBOAs) correlated well with BrC light absorption (Xie et

559   al., 2018;Qin et al., 2018). Thus, the significant correlation between BrC absorption and K$^+$

560   reaffirmed that biomass burning was the crucial emission source of BrC observed in this work.

561   Although the geographic location of the observation site was situated in a coastal area and K$^+$

562   could also be found in sea salt (Pio et al., 2008), it should be noted that the prevailing wind

563   direction during winter was from the north (see Fig. 3), which drives maritime air parcels away

564   from the site. Hence, the effect of sea salt and crustal materials to K$^+$ was slight, which was

565   demonstrated in the supplementary information as shown in Fig. S7. Other earlier studies also

566   suggested that the sea salt contribution to the K$^+$ concentrations of PM$_{2.5}$ was trivial in the PRD

567   region during the winter (Lai et al., 2007). Another possible K$^+$ source was coal combustion.

568   The coal consumption in the PRD region was dominated by coal-fired power plants. The

569   emission from power plants was usually very steady and was less likely to affect the diurnal

570   correlation between K$^+$ and BrC absorption. As shown in Fig. S8, the ratios of K$^+$/PM$_{2.5}$ varies

571   approximately from 0.015 and 0.020 and the diurnal profile of K$^+$/PM$_{2.5}$ shows very little

572   variation. Yu et al. (2018) have suggested that K$^+$ usually accounted for 2.34-5.49% of PM$_{2.5}$ in

573   the laboratory biomass burning study. However, K$^+$ was normally lower than 1% of coal

574   combustion PM$_{2.5}$. Therefore, the ratio range of K$^+$ to PM$_{2.5}$ observed in this work likely

575   indicated aged biomass burning particles. Both nitrogen oxides (NO$_x$) and ammonia (NH$_3$) can

576 be found in biomass burning plumes (Andreae and Merlet, 2001). For NO_3^- and NH_4^+, nitrate

577 can be converted from NO_x through atmospheric reactions, and ammonium may originate from

578 NH_3. However, similar to the diurnal variation in $\sigma_{abs,BrC,370nm}$, diurnal variations in NH_4^+ and

579 NO_3^- also increased in the afternoon and appeared at nighttime in Fig S8. However, $NO_3^-/PM_{2.5}$

580 and $NH_4^+/PM_{2.5}$ reached their peaks at noon, indicating that ammonium nitrate formed from the

581 secondary reaction at this time. Along with the reduced boundary layer height and ambient

582 temperature, NO_3^- was accumulated until the photochemical reaction stopped at night. The

583 diurnal variation in NH_4^+ was similar to that in NO_3^- due to the acid/base neutralization reaction.

584 The overlapping of the $\sigma_{abs,BrC,370nm}$, NH_4^+ and NO_3^- diurnal variations would lead to a significant

585 correlation between BrC absorption and NO_3^- or NH_4^+. High concentrations of Ca^{2+} and Mg^{2+}

586 are often found in dust-related aerosols (Lee et al., 1999). $\sigma_{abs,BrC,370nm}$ showed poor correlations

587 with both Ca^{2+} and Mg^{2+}, indicating that dust-related aerosol components contribute

588 insignificantly to the total aerosol mass loading and, thus, dust may not affect the AAE

589 differentiation method used in this work. Although sulfur dioxide (SO_2) may also be emitted by

590 biomass burning, SO_4^{2-} is often believed to be secondary in nature, and the presence of other

591 intense SO_2 sources (e.g., automobile and industrial emissions) further reduces the correlation

592 between BrC and SO_4^{2-}. Sources of Cl^- include both combustion and sea salt spray (Waldman

593 et al., 1991). Although the prevailing wintertime wind direction was from the north, sea salt

594 can still be carried to the site by a weak sea breeze, and thus, Cl^- may not show considerable

595 correlation with BrC.

596 **3.4 BrC radiative forcing efficiency**

597 The radiative effects of aerosol scattering, BrC absorption, and BC absorption were investigated

598 by the SBDART model. For each investigated variable under cloud-free conditions, we run the

599 model twice to calculate the DRF at the TOA with and without the investigated variable.

600 Accordingly, the difference of ΔF between the two simulations was considered as the radiative

601 effect of the investigated variable. The results showed that the average radiative forcings at the

602 TOA by scattering, BrC absorption, and BC absorption were -21.4±5.5 W m^{-2}, 2.3±1.8 W m^{-2},

603 and 10.9±5.1 W m^{-2}, respectively. Furthermore, BrC absorption was attributed to 15.8±4.4%

604 of the warming effect caused by aerosol light absorption, demonstrating the nonnegligible role

605 of BrC in radiative forcing evaluation.

606   We also calculated the BrC radiative forcing efficiency (RFE) under various SSA (ranging from

607   0.7 to 0.99) at three wavelengths, i.e., 440 nm, 675 nm, and 870 nm. The RFE was denoted as

608   the radiative forcing normalized by the AOD. The average AOD and ASY at the three

609   wavelengths were 0.365 and 0.691 at 440 nm, 0.212 and 0.632 at 675 nm, and 0.154 and 0.619

610   at 870 nm, respectively. A solar zenith angle of 55° and an average shortwave broadband surface

611   albedo (0.119) were used in the calculation. The results were plotted as a set of RFE lookup

612   charts as a function of the surface BrC absorption contribution (see Fig. 9).

613   In general, for any wavelength, the RFE increased with increasing BrC absorption contribution

614   for a certain SSA, indicating that BrC was a more efficient radiative forcing agent due to the

615   preferential absorbance of BrC in a shorter wavelength range. However, for a certain BrC

616   absorption contribution, the RFE increased with decreasing SSA, i.e., a higher portion of light-

617   absorbing aerosol components can lead to more efficient radiative forcing. The trend among

618   panels (a), (b), and (c) in Fig. 9 demonstrated that the effect of BrC absorption contribution on

619   RFE was wavelength-dependent, i.e., BrC was a weaker radiative forcing agent at longer

620   wavelengths, which is also consistent with the wavelength-dependent light-absorbing property

621   of BrC. The red stars in Fig. 9 denote the average SSA and BrC absorption contribution

622   conditions during this campaign, i.e., 0.029 W m^{-2} per unit AOD at 440 nm (Fig. 9a), 0.007 W

623   m^{-2} per unit AOD at 675 nm (Fig. 9b), and 0.0002 W m^{-2} per unit AOD at 870 nm (Fig. 9c).

624   These results suggested that the average value of RFE decreased distinctly from 440 nm to 870

625   nm not only because of the lower BrC absorption contribution but also because of the

626   wavelength-dependence of the BrC RFE. It should also be noted that the simulations were based

627   on SSA measured under dry conditions. Under the typical ambient conditions of the PRD, the

628   SSA might be markedly enhanced by aerosol water uptake (Jung et al., 2009), and then, the BrC

629   radiative forcing efficiency might be less. Moreover, Fig. 9 also serves as a lookup table to

630   conveniently assess the BrC radiative forcing efficiency at different wavelengths with different

631   BrC absorption contributions for a certain SSA.

632   **4 Conclusion**

633   In this work, light absorption due to BrC in the PRD region of China was quantitatively deduced

634   during the winter season of 2014. The AAE of ambient particles and BC core were derived

635   from the measurements. For ambient particles, $AAE_{370-520nm}$ and $AAE_{520-880nm}$ ranged from 0.81

636 to 2.31 and 0.91 to 2.13, respectively. In the case of BC, $AAE_{BC,370-520nm}$ and $AAE_{BC,520-880nm}$

637 ranged from 0.59 to 0.98 and 0.82 to 1.15, respectively. Using the absorption coefficients of

638 BC calculated according to the Mie theory and the observed total aerosol absorption coefficients,

639 we estimated the AAE_{BC} and hence the BrC absorption contribution for the optically equivalent

640 mixture configuration. The average BrC light absorption contribution ranged from 8.7±4.3% at

641 660 nm up to 34.1±8.0% at 370 nm when AAE_{BC} was set as uniform. The sensitivity of AAE_{BC}

642 estimation associated with different RI and mixing state assumptions was further investigated.

643 The results showed that variations in the real RI of the non-absorbing material (1.35 to 1.6) may

644 decrease $AAE_{BC,370-520nm}$ from 0.84 to 0.87 and $AAE_{BC,520-880nm}$ from 1.07 to 1.15 for core-shell

645 mixtures, with an $AAE_{BC,370-520nm}$ of 0.33 and $AAE_{BC,520-880nm}$ of 0.63 for external mixtures.

646 Variations in the core's real RI (1.5 to 2.0) and imaginary RI (0.4 to 1.0) may reduce $AAE_{BC,370-520nm}$

647 $_{520nm}$ from 0.55 to 0.99 and $AAE_{BC,520-880nm}$ from 0.84 to 1.27 for the core-shell mixture and

648 reduce $AAE_{BC,370-520nm}$ from 0.04 to 0.45 and $AAE_{BC,520-880nm}$ from 0.28 to 0.79 for the external

649 mixture. These results indicate that the optical properties of the BC core and non-absorbing

650 material can significantly affect the accuracy of AAE_{BC} and corresponding BrC absorption

651 contribution estimations. Compared to the values of BrC light absorption coefficient and BrC

652 light absorption contribution from other similar studies conducted in the East Asia region, the

653 BrC measured in this work showed relatively lower values of light absorption coefficient but

654 was found responsible for relatively higher portion of light absorption. It should be noted that

655 the calculated BrC light absorption may vary exponentially with the value of AAE_{BC}. According

656 to Monte Carlo simulations under 95% confidence level, we found that BrC light absorption

657 contribution ratios in this work can range roughly from 18% to 48% at 370 nm, 10% to 37% at

658 470 nm, 3% to 27% at 520 nm, 3% to 22% at 590 nm, and 1% to 16% at 660 nm, respectively.

659 Therefore, proper values of AAE_{BC} have to be carefully obtained for a particular study area,

660 especially needed to be constrained by the BC mass concentration, size-distribution, and mixing

661 state measurements.

662 Additionally, the measurements of major water-soluble inorganic ions (including K^+, NO_3^-, and

663 NH_4^+) and particulate OC showed consistent features with those of $\sigma_{abs,BrC,370nm}$, implying that

664 BrC was associated with biomass-burning emissions from nearby rural areas. Moreover, the

665 diurnal trend in $\sigma_{abs,BrC,370nm}$/OC indicated that primary biomass burning emissions can produce

666 intense light-absorbing BrC, while the photochemical aging process may weaken the light-

667 absorbing capability of BrC.

668 Using a radiative transfer model (i.e., SBDART), we estimated the BrC effects on aerosol

669 radiative forcing. The average shortwave aerosol direct radiative forcings due to scattering, BrC

670 absorption, and BC absorption at the TOA were evaluated to be -21.4±5.5 W m^{-2}, 2.3±1.8 W

671 m^{-2}, and 10.9±5.1 W m^{-2}, respectively. BrC absorption accounted for 15.8±4.4% of the total

672 shortwave solar absorption warming effect at the TOA, indicating that BrC might be an

673 important climate forcing agent, which is largely neglected in current climate models. To

674 facilitate the estimation of the climate effects of BrC, a set of look-up charts was constructed

675 for the investigated area based on the default tropical atmosphere profile, average surface

676 albedo, average asymmetry factor, and surface-measured aerosol properties (i.e., BrC

677 absorption contribution, *SSA*, and AOD). Therefore, the role of the BrC radiative forcing

678 efficiency at three wavelengths can be conveniently assessed for certain *SSA* and BrC

679 absorption contributions.

680

681 *Author contributions*

682 HT, JZ, YM, and CC designed the experiments, and ZL, LL, YQ, NW, FL, YL, and MC carried

683 out the field measurements and data analysis. ZL and YQ performed Mie theory simulation.

684 ZL, JZ, and HT prepared the manuscript with comments from all coauthors.

685

686 *Acknowledgements*

687 This work is supported by the National Key Project of MOST (2016YFC0201901 and

688 2016YFC0203305), and National Natural Science Foundation of China (41575122 and

689 41730106). We are also deeply thankful for Dr. Wu and the staff at the Hong Kong Polytechnic

690 University site of AERONET.

691

692 **References:**
693 Andreae, M. O., and Merlet, P.: Emission of trace gases and aerosols from biomass burning,
694 Glob. Biogeochem. Cycle, 15, 955-966, 2001.

695 Andreae, M. O., and Gelencser, A.: Black carbon or brown carbon? The nature of light-

696   absorbing carbonaceous aerosols, Atmospheric Chemistry & Physics, 6, 3131-3148, 2006.

697   Ångström, A.: On the Atmospheric Transmission of Sun Radiation and on Dust in the Air,
698   Geografiska Annaler, 11, 156-166, 1929.

699   Arnott, W. P., Hamasha, K., Moosmüller, H., Sheridan, P. J., and Ogren, J. A.: Towards Aerosol
700   Light-Absorption Measurements with a 7-Wavelength Aethalometer: Evaluation with a
701   Photoacoustic Instrument and 3-Wavelength Nephelometer, Aerosol Science and Technology,
702   39, 17-29, 10.1080/027868290901972, 2005.

703   Arola, A., Schuster, G. L., Pitkänen, M. R. A., Dubovik, O., Kokkola, H., Lindfors, A. V.,
704   Mielonen, T., Raatikainen, T., Romakkaniemi, S., Tripathi, S. N., and Lihavainen, H.: Direct
705   radiative effect by brown carbon over the Indo-Gangetic Plain, Atmospheric Chemistry and
706   Physics, 15, 12731-12740, 10.5194/acp-15-12731-2015, 2015.

707   Bauer, J. J., Yu, X.-Y., Cary, R., Laulainen, N., and Berkowitz, C.: Characterization of the
708   Sunset Semi-Continuous Carbon Aerosol Analyzer, Journal of the Air & Waste Management
709   Association, 59, 826-833, 10.3155/1047-3289.59.7.826, 2012.

710   Bodhaine, B. A.: Aerosol absorption measurements at Barrow, Mauna Loa and the south pole,
711   Journal of Geophysical Research Atmosperes, 100, 8967–8975, 1995.

712   Bohren, C. F., and Huffman, D. R.: Wiley: Absorption and Scattering of Light by Small
713   Particles - Craig F. Bohren, Donald R. Huffman, Optics & Laser Technology, 31, 328-328, 1983.

714   Bohren, C. F., and Huffman, D. R.: Absorption and Scattering of Light by Small Particles,
715   WILEY‐VCH Verlag GmbH & Co. KGaA 328-328 pp., 2007.

716   Bond, T. C., Streets, D. G., Yarber, K. F., Nelson, S. M., Woo, J. H., and Klimont, Z.: A
717   technology-based global inventory of black and organic carbon emissions from combustion, J.
718   Geophys. Res.-Atmos., 109, 43, 10.1029/2003jd003697, 2004.

719   Bond, T. C., Zarzycki, C., Flanner, M. G., and Koch, D. M.: Quantifying immediate radiative
720   forcing by black carbon and organic matter with the Specific Forcing Pulse, Atmospheric
721   Chemistry and Physics, 11, 1505-1525, 10.5194/acp-11-1505-2011, 2011.

722   Bricaud, A., and Morel, A.: Light attenuation and scattering by phytoplanktonic cells: a
723   theoretical modeling, Applied Optics, 25, 571, 10.1364/ao.25.000571, 1986.

724   Burling, I. R., Yokelson, R. J., Akagi, S. K., Urbanski, S. P., Wold, C. E., Griffith, D. W. T.,
725   Johnson, T. J., Reardon, J., and Weise, D. R.: Airborne and ground-based measurements of the
726   trace gases and particles emitted by prescribed fires in the United States (vol 11, pg 12197,
727   2011), Atmospheric Chemistry and Physics, 12, 103-103, 10.5194/acp-12-103-2012, 2012.

728   Chan, C. K., and Yao, X.: Air pollution in mega cities in China, Atmospheric Environment, 42,
729   1-42, http://dx.doi.org/10.1016/j.atmosenv.2007.09.003, 2008.

730   Cheng, Y., He, K. B., Zheng, M., Duan, F. K., Du, Z. Y., Ma, Y. L., Tan, J. H., Yang, F. M., Liu,
731   J. M., Zhang, X. L., Weber, R. J., Bergin, M. H., and Russell, A. G.: Mass absorption efficiency
732   of elemental carbon and water-soluble organic carbon in Beijing, China, Atmospheric
733   Chemistry and Physics, 11, 11497-11510, 10.5194/acp-11-11497-2011, 2011.

734   Cheng, Y. F., Eichler, H., Wiedensohler, A., Heintzenberg, J., Zhang, Y. H., Hu, M., Herrmann,
735   H., Zeng, L. M., Liu, S., Gnauk, T., Brüggemann, E., and He, L. Y.: Mixing state of elemental
736   carbon and non-light-absorbing aerosol components derived from in situ particle optical
737   properties at Xinken in Pearl River Delta of China, Journal of Geophysical Research:
738   Atmospheres, 111, doi:10.1029/2005JD006929, 2006.

739   Cheung, H. H. Y., Tan, H., Xu, H., Li, F., Wu, C., Yu, J. Z., and Chan, C. K.: Measurements of
740   non-volatile aerosols with a VTDMA and their correlations with carbonaceous aerosols in
741   Guangzhou, China, Atmospheric Chemistry and Physics, 16, 8431-8446, 10.5194/acp-16-
742   8431-2016, 2016.

743   Coen, M. C., Weingartner, E., Apituley, A., Ceburnis, D., Fierzschmidhauser, R., Flentje, H.,
744   Henzing, J. S., Jennings, S. G., Moerman, M., and Petzold, A.: Minimizing light absorption
745   measurement artifacts of the Aethalometer: evaluation of five correction algorithms,
746   Atmospheric Measurement Techniques, 3, 457-474, 2010.

747   Desyaterik, Y., Sun, Y., Shen, X., Lee, T., Wang, X., Wang, T., and Collett, J. L.: Speciation of
748   "brown" carbon in cloud water impacted by agricultural biomass burning in eastern China,
749   Journal of Geophysical Research: Atmospheres, 118, 7389-7399, 10.1002/jgrd.50561, 2013.

750   Drinovec, L., Močnik, G., Zotter, P., Prévôt, A. S. H., Ruckstuhl, C., Coz, E., Rupakheti, M.,
751   Sciare, J., Müller, T., Wiedensohler, A., and Hansen, A. D. A.: The "dual-spot" Aethalometer:
752   an improved measurement of aerosol black carbon with real-time loading compensation,
753   Atmospheric Measurement Techniques, 8, 1965-1979, 10.5194/amt-8-1965-2015, 2015.

754   Erlick, C., Abbatt, J. P. D., and Rudich, Y.: How Different Calculations of the Refractive Index
755   Affect Estimates of the Radiative Forcing Efficiency of Ammonium Sulfate Aerosols, Journal
756   of the Atmospheric Sciences, 68, 1845-1852, 10.1175/2011jas3721.1, 2011.

757   Feng, X., Dang, Z., Huang, W., Shao, L., and Li, W.: Microscopic morphology and size
758   distribution of particles in PM2.5 of Guangzhou City, J Atmos Chem, 64, 37-51,
759   10.1007/s10874-010-9169-7, 2010.

760   Feng, Y., Ramanathan, V., and Kotamarthi, V. R.: Brown carbon: a significant atmospheric
761   absorber of solar radiation?, Atmospheric Chemistry and Physics, 13, 8607-8621, 10.5194/acp-
762   13-8607-2013, 2013.

763   Hoffer, A., Gelencsér, A., Guyon, P., and Kiss, G.: Optical properties of humic-like substances
764   (HULIS) in biomass-burning aerosols, Atmospheric Chemistry & Physics, 5, 3563-3570, 2005.

765   Holben, B. N., Eck, T. F., Slutsker, I., Tanré, D., Buis, J. P., Setzer, A., Vermote, E., Reagan, J.
766   A., Kaufman, Y. J., and Nakajima, T.: AERONET—A Federated Instrument Network and Data

767   Archive for Aerosol Characterization, Remote Sensing of Environment, 66, 1-16, 1998.

768   Huang, R.-J., Zhang, Y., Bozzetti, C., Ho, K.-F., Cao, J.-J., Han, Y., Daellenbach, K. R., Slowik,
769   J. G., Platt, S. M., Canonaco, F., Zotter, P., Wolf, R., Pieber, S. M., Bruns, E. A., Crippa, M.,
770   Ciarelli, G., Piazzalunga, A., Schwikowski, M., Abbaszade, G., Schnelle-Kreis, J.,
771   Zimmermann, R., An, Z., Szidat, S., Baltensperger, U., Haddad, I. E., and Prévôt, A. S. H.:
772   High secondary aerosol contribution to particulate pollution during haze events in China,
773   Nature, 514, 218-222, 10.1038/nature13774, 2014.

774   Jiang, D., Wang, C., Wu, D., Deng, X., Huang, X., Tan, H., Li, F., and Deng, T.: Diurnal
775   variation of atmospheric boundary layer over Wushan station, Guangzhou using wind profiler
776   radar (in Chinese), Journal of Tropical Meteorology, 29, 129-135, 2013.

777   Jung, J., Lee, H., Kim, Y. J., Liu, X., Zhang, Y., Gu, J., and Fan, S.: Aerosol chemistry and the
778   effect of aerosol water content on visibility impairment and radiative forcing in Guangzhou
779   during the 2006 Pearl River Delta campaign, Journal of Environmental Management, 90, 3231-
780   3244, http://dx.doi.org/10.1016/j.jenvman.2009.04.021, 2009.

781   Katrinak, K. A., Rez, P., Perkes, P. R., and Buseck, P. R.: Fractal geometry of carbonaceous
782   aggregates from an urban aerosol, Environmental Science & Technology, 27, págs. 225-238,
783   1993.

784   Khalizov, A. F., Xue, H., Wang, L., Zheng, J., and Zhang, R.: Enhanced light absorption and
785   scattering by carbon soot aerosol internally mixed with sulfuric acid, The journal of physical
786   chemistry. A, 113, 1066-1074, 10.1021/jp807531n, 2009.

787   Kirchstetter, T. W., Novakov, T., and Hobbs, P. V.: Evidence that the spectral dependence of
788   light absorption by aerosols is affected by organic carbon, Journal of Geophysical Research:
789   Atmospheres, 109, n/a-n/a, 10.1029/2004jd004999, 2004.

790   Kulkarni, P., Baron, P. A., and Willeke, K.: Aerosol measurement : principles, techniques, and
791   applications, Van Nostrand Reinhold, 807-808 pp., 1996.

792   Lack, D. A., and Cappa, C. D.: Impact of brown and clear carbon on light absorption
793   enhancement, single scatter albedo and absorption wavelength dependence of black carbon,
794   Atmospheric Chemistry and Physics, 10, 4207-4220, 10.5194/acp-10-4207-2010, 2010.

795   Lack, D. A., and Langridge, J. M.: On the attribution of black and brown carbon light absorption
796   using the Ångström exponent, Atmospheric Chemistry and Physics, 13, 10535-10543,
797   10.5194/acp-13-10535-2013, 2013.

798   Lai, S.-c., Zou, S.-c., Cao, J.-j., Lee, S.-c., and Ho, K.-f.: Characterizing ionic species in PM2.5
799   and PM10 in four Pearl River Delta cities, South China, Journal of Environmental Sciences, 19,
800   939-947, https://doi.org/10.1016/S1001-0742(07)60155-7, 2007.

801   Laskin, A., Laskin, J., and Nizkorodov, S. A.: Chemistry of atmospheric brown carbon, Chem
802   Rev, 115, 4335-4382, 10.1021/cr5006167, 2015.

803 Lee, E., Chan, C. K., and Paatero, P.: Application of positive matrix factorization in source
804 apportionment of particulate pollutants in Hong Kong, Atmospheric Environment, 33, 3201-
805 3212, https://doi.org/10.1016/S1352-2310(99)00113-2, 1999.

806 Levine, J.: Biomass Burning Aerosols in a Savanna Region of the Ivory Coast, French Forum,
807 235-236, 1991.

808 Li, H., Han, Z., Cheng, T., Du, H., Kong, L., Chen, J., Zhang, R., and Wang, W.: Agricultural
809 Fire Impacts on the Air Quality of Shanghai during Summer Harvesttime, Aerosol and Air
810 Quality Research, 10.4209/aaqr.2009.08.0049, 2010.

811 Lin, P., Hu, M., Deng, Z., Slanina, J., Han, S., Kondo, Y., Takegawa, N., Miyazaki, Y., Zhao,
812 Y., and Sugimoto, N.: Seasonal and diurnal variations of organic carbon in PM2.5in Beijing
813 and the estimation of secondary organic carbon, Journal of Geophysical Research, 114,
814 10.1029/2008jd010902, 2009.

815 Liu, C., Chung, C. E., Yin, Y., and Schnaiter, M.: The absorption Ångström exponent of black
816 carbon: from numerical aspects, Atmospheric Chemistry and Physics, 18, 6259-6273,
817 10.5194/acp-18-6259-2018, 2018.

818 Liu, D., Taylor, J. W., Young, D. E., Flynn, M. J., Coe, H., and Allan, J. D.: The effect of
819 complex black carbon microphysics on the determination of the optical properties of brown
820 carbon, Geophysical Research Letters, 42, 613-619, 2015.

821 Liu, L., Mishchenko, M. I., and Patrick Arnott, W.: A study of radiative properties of fractal
822 soot aggregates using the superposition T-matrix method, Journal of Quantitative Spectroscopy
823 and Radiative Transfer, 109, 2656-2663, 10.1016/j.jqsrt.2008.05.001, 2008.

824 Ma, N., Zhao, C. S., Müller, T., Cheng, Y. F., Liu, P. F., Deng, Z. Z., Xu, W. Y., Ran, L., Nekat,
825 B., van Pinxteren, D., Gnauk, T., Müller, K., Herrmann, H., Yan, P., Zhou, X. J., and
826 Wiedensohler, A.: A new method to determine the mixing state of light absorbing carbonaceous
827 using the measured aerosol optical properties and number size distributions, Atmos. Chem.
828 Phys., 12, 2381-2397, 10.5194/acp-12-2381-2012, 2012.

829 Ma, Y., Li, S. Z., Zheng, J., Khalizov, A., Wang, X., Wang, Z., and Zhou, Y. Y.: Size-resolved
830 measurements of mixing state and cloud-nucleating ability of aerosols in Nanjing, China, J.
831 Geophys. Res.-Atmos., 122, 9430-9450, 10.1002/2017jd026583, 2017.

832 Mie, G.: Beitrage Zur Optik Truber Medien, Speziell Kolloidaler Metallosungen, Annalen Der
833 Physik, 25, 377, 1908.

834 Moosmüller, H., Chakrabarty, R. K., Ehlers, K. M., and Arnott, W. P.: Absorption Ångström
835 coefficient, brown carbon, and aerosols: basic concepts, bulk matter, and spherical particles,
836 Atmospheric Chemistry and Physics, 11, 1217-1225, 10.5194/acp-11-1217-2011, 2011.

837 Nakayama, T., Ikeda, Y., Sawada, Y., Setoguchi, Y., Ogawa, S., Kawana, K., Mochida, M.,
838 Ikemori, F., Matsumoto, K., and Matsumi, Y.: Properties of light‐absorbing aerosols in the

839 Nagoya urban area, Japan, in August 2011 and January 2012: Contributions of brown carbon
840 and lensing effect, Journal of Geophysical Research Atmospheres, 119, 12,721-712,739, 2015.

841 Olson, M. R., Victoria Garcia, M., Robinson, M. A., Van Rooy, P., Dietenberger, M. A., Bergin,
842 M., and Schauer, J. J.: Investigation of black and brown carbon multiple-wavelength-dependent
843 light absorption from biomass and fossil fuel combustion source emissions, Journal of
844 Geophysical Research: Atmospheres, 120, 6682-6697, 10.1002/2014jd022970, 2015.

845 Pio, C. A., Legrand, M., Alves, C. A., Oliveira, T., Afonso, J., Caseiro, A., Puxbaum, H.,
846 Sanchez-Ochoa, A., and Gelencsér, A.: Chemical composition of atmospheric aerosols during
847 the 2003 summer intense forest fire period, Atmospheric Environment, 42, 7530-7543, 2008.

848 Qin, Y. M., Tan, H. B., Li, Y. J., Li, Z. J., Schurman, M. I., Liu, L., Wu, C., and Chan, C. K.:
849 Chemical characteristics of brown carbon in atmospheric particles at a suburban site near
850 Guangzhou, China, Atmospheric Chemistry and Physics Discussions, 1-23, 10.5194/acp-2018-
851 730, 2018.

852 Redmond, H., and Thompson, J. E.: Evaluation of a quantitative structure-property relationship
853 (QSPR) for predicting mid-visible refractive index of secondary organic aerosol (SOA),
854 Physical chemistry chemical physics : PCCP, 13, 6872-6882, 10.1039/c0cp02270e, 2011.

855 Ricchiazzi, P., Yang, S., Gautier, C., and Sowle, D.: SBDART: A Research and Teaching
856 Software Tool for Plane-Parallel Radiative Transfer in the Earth's Atmosphere, Bulletin of the
857 American Meteorological Society, 79, 2101-2114, 10.1175/1520-
858 0477(1998)079<2101:Sarats>2.0.Co;2, 1998.

859 Roesch, A.: Use of Moderate-Resolution Imaging Spectroradiometer bidirectional reflectance
860 distribution function products to enhance simulated surface albedos, Journal of Geophysical
861 Research, 109, 10.1029/2004jd004552, 2004.

862 Sareen, N., Schwier, A. N., Shapiro, E. L., Mitroo, D., and McNeill, V. F.: Secondary organic
863 material formed by methylglyoxal in aqueous aerosol mimics, Atmospheric Chemistry and
864 Physics, 10, 997-1016, 10.5194/acp-10-997-2010, 2010.

865 Satish, R., Shamjad, P., Thamban, N., Tripathi, S., and Rastogi, N.: Temporal Characteristics of
866 Brown Carbon over the Central Indo-Gangetic Plain, Environ Sci Technol, 51, 6765-6772,
867 10.1021/acs.est.7b00734, 2017.

868 Scarnato, B. V., Nielsen, K., Vahidinia, S., and Richard, D.: Effect of Aggregation and Mixing
869 on optical properties of Black Carbon, 2013.

870 Schmid, O., Artaxo, P., Arnott, W. P., Chand, D., Gatti, L. V., Frank, G. P., Hoffer, A., Schnaiter,
871 M., and Andreae, M. O.: Spectral light absorption by ambient aerosols influenced by biomass
872 burning in the Amazon Basin. I: Comparison and field calibration of absorption measurement
873 techniques, Atmos. Chem. Phys., 6, 3443-3462, 10.5194/acp-6-3443-2006, 2006.

874 Segura, S., Estellés, V., Titos, G., Lyamani, H., Utrillas, M. P., Zotter, P., Prévôt, A. S. H.,

875 Močnik, G., Alados-Arboledas, L., and Martínez-Lozano, J. A.: Determination and analysis of
876 in situ spectral aerosol optical properties by a multi-instrumental approach, Atmospheric
877 Measurement Techniques, 7, 2373-2387, 10.5194/amt-7-2373-2014, 2014.

878 Seinfeld, J. H., and Pandis, S. N.: Atmospheric Chemistry and Physics, John Wiley & Sons, Inc,
879 New York, 1998.

880 Stokes, G. M., and Schwartz, S. E.: The Atmospheric Radiation Measurement (ARM) Program:
881 Programmatic Background and Design of the Cloud and Radiation Test Bed, Bulletin of the
882 American Meteorological Society, 75, 1201–1221, 1994.

883 T. C. Bond, †, M. Bussemer, B. Wehner, S. Keller, R. J. Charlson, a., and Heintzenberg‡, J.:
884 Light Absorption by Primary Particle Emissions from a Lignite Burning Plant, Environmental
885 Science & Technology, 33, 3887-3891, 1999.

886 Tan, H., Liu, L., Fan, S., Li, F., Yin, Y., Cai, M., and Chan, P. W.: Aerosol optical properties and
887 mixing state of black carbon in the Pearl River Delta, China, Atmospheric Environment, 131,
888 196-208, http://dx.doi.org/10.1016/j.atmosenv.2016.02.003, 2016a.

889 Tan, H., Yin, Y., Li, F., Liu, X., Chan, P. W., Deng, T., Deng, X., Wan, Q., and Wu, D.:
890 Measurements of particle number size distributions and new particle formations events during
891 winter in the Pearl River Delta region, China, Journal of Tropical Meteorology, 22, 191-199,
892 10.16555/j.1006-8775.2016.02.009, 2016b.

893 Waldman, J. M., Lioy, P. J., Zelenka, M., Jing, L., Lin, Y. N., He, Q. C., Qian, Z. M., Chapman,
894 R., and Wilson, W. E.: Wintertime measurements of aerosol acidity and trace elements in
895 Wuhan, a city in central China, Atmospheric Environment. Part B. Urban Atmosphere, 25, 113-
896 120, https://doi.org/10.1016/0957-1272(91)90045-G, 1991.

897 Wang, J., Nie, W., Cheng, Y., Shen, Y., Chi, X., Wang, J., Huang, X., Xie, Y., Sun, P., Xu, Z.,
898 Qi, X., Su, H., and Ding, A.: Light absorption of brown carbon in eastern China based on 3-
899 year multi-wavelength aerosol optical property observations and an improved absorption
900 Ångström exponent segregation method, Atmospheric Chemistry and Physics, 18, 9061-9074,
901 10.5194/acp-18-9061-2018, 2018.

902 Washenfelder, R. A., Attwood, A. R., Brock, C. A., Guo, H., Xu, L., Weber, R. J., Ng, N. L.,
903 Allen, H. M., Ayres, B. R., and Baumann, K.: Biomass burning dominates brown carbon
904 absorption in the rural southeastern United States, Geophysical Research Letters, 42, 653-664,
905 2015.

906 Wex, H., Neusüß, C., Wendisch, M., Stratmann, F., Koziar, C., Keil, A., Wiedensohler, A., and
907 Ebert, M.: Particle scattering, backscattering, and absorption coefficients: An in situ closure
908 and sensitivity study, Journal of Geophysical Research Atmospheres, 107, LAC-1-LAC 4-18,
909 2002.

910 Wu, C., Wu, D., and Yu, J. Z.: Quantifying black carbon light absorption enhancement with
911 a novel statistical approach, Atmospheric Chemistry and Physics, 18, 289-309, 10.5194/acp-

18-289-2018, 2018.

Wu, D., Mao, J., Deng, X., Tie, X., Zhang, Y., Zeng, L., Li, F., Tan, H., Bi, X., Huang, X., Chen, J., and Deng, T.: Black carbon aerosols and their radiative properties in the Pearl River Delta region, Science in China Series D: Earth Sciences, 52, 1152-1163, 10.1007/s11430-009-0115-y, 2009.

Xie, C., Xu, W., Wang, J., Wang, Q., Liu, D., Tang, G., Chen, P., Du, W., Zhao, J., Zhang, Y., Zhou, W., Han, T., Bian, Q., Li, J., Fu, P., Wang, Z., Ge, X., Allan, J., Coe, H., and Sun, Y.: Vertical characterization of aerosol optical properties and brown carbon in winter in urban Beijing, China, Atmospheric Chemistry and Physics Discussions, 1-28, 10.5194/acp-2018-788, 2018.

Yu, J., Yan, C., Liu, Y., Li, X., Zhou, T., and Zheng, M.: Potassium: A Tracer for Biomass Burning in Beijing?, Aerosol and Air Quality Research, 18, 2447-2459, 10.4209/aaqr.2017.11.0536, 2018.

Yuan, J. F., Huang, X. F., Cao, L. M., Cui, J., Zhu, Q., Huang, C. N., Lan, Z. J., and He, L. Y.: Light absorption of brown carbon aerosol in the PRD region of China, Atmospheric Chemistry and Physics, 16, 1433-1443, 10.5194/acp-16-1433-2016, 2016a.

Yuan, L., Yin, Y., Xiao, H., Yu, X., Hao, J., Chen, K., and Liu, C.: A closure study of aerosol optical properties at a regional background mountainous site in Eastern China, Science of The Total Environment, 550, 950-960, 10.1016/j.scitotenv.2016.01.205, 2016b.

Zhang, Y., Li, Z., Sun, Y., Lv, Y., and Xie, Y.: Estimation of atmospheric columnar organic matter (OM) mass concentration from remote sensing measurements of aerosol spectral refractive indices, Atmospheric Environment, 179, 107-117, 10.1016/j.atmosenv.2018.02.010, 2018.

Zhou, S., Wang, T., Wang, Z., Li, W., Xu, Z., Wang, X., Yuan, C., Poon, C. N., Louie, P. K. K., Luk, C. W. Y., and Wang, W.: Photochemical evolution of organic aerosols observed in urban plumes from Hong Kong and the Pearl River Delta of China, Atmospheric Environment, 88, 219-229, 10.1016/j.atmosenv.2014.01.032, 2014.

941 **Table 1.** Inter-comparison of the performance of various Mie-calculation schemes. The base

942 case is based on the empirical distribution function and mixing states of BC particles obtained

943 from previous field measurements at the same site. $\Phi_{N,CV}$ denotes the portion of non-BC

944 particles and r_{ext} is the mass portion of externally mixed BC with respect to total BC. AAE_{BC} is

945 the absorption Ångström exponent of BC, and the subscript represents the wavelength range.

946 $Abs_{BrC,370}\%$ and $Abs_{BrC,520}\%$ are the BrC absorption contributions at 370 nm and 520 nm,

947 respectively. $Calcabs_{880}$ is the calculated absorption at 880 nm using Mie model. $Measabs_{880}$ is

948 the measured absorption by an Aethalometer at 880 nm. b is the intercept of the regression

949 analysis between $Measabs_{880}$ and $Calcabs_{880}$, i.e., $Calcabs_{880}=b*Measabs_{880}$. R^2 is the

950 correlation coefficient of the equation. The refractive index of BC core ($\tilde{m}_{core}$) and nonlight-

951 absorbing particles ($\tilde{m}_{non}$) is set to be 1.80-0.54i and $1.55-10^{-7}$i, respectively (Tan et al., 2016a),

Case #	Scheme	$\Phi_{N,CV}$	r_{ext}	AAE $_{BC,370-520}$	AAE $_{BC,520-880}$	Abs $_{BrC,370}\%$	Abs $_{BrC,520}\%$	Calc abs$_{880}$	Meas abs$_{880}$	b	R^2
Base		0.384 to 0.137	0.58	0.723	0.962	34.13%	15.96%	21.869		1.019	0.979
1		0	1	0.331	0.626	51.64%	29.57%	15.832		0.747	0.968
2		0	0	0.856	1.128	24.76%	8.28%	27.827		1.295	0.976
3		0	0.58	0.745	0.974	33.22%	15.46%	21.936	**21.199**	1.029	0.979
4		0.384 to 0.137	0	0.835	1.111	26.01%	9.14%	27.302		1.269	0.975
5		0.5	0	0.778	1.043	29.96%	12.30%	24.921		1.150	0.968
6		0.5	0.58	0.674	0.928	36.39%	17.49%	20.897		0.977	0.975

952

953

954

955 **Table 2.** Observational studies of the BrC light absorption coefficient and contribution in the

956 near-ultraviolet wavelength range in East Asia.

Periods	Location	λ (nm)	Mean BrC absorption coefficient	Mean BrC absorption contribution	Instrumentation	Reference
Nov. 2014 – Jan. 2015	Guangzhou (China)	370	17.6 Mm^{-1} 23.5 Mm^{-1}	26.2% (AAE$_{BC}$=1) 34.1% (corrected)	Aethalometer AE-33	This study
Jan. 2014 – Feb. 2014; Sep. 2014 – Oct. 2014	Shenzhen (China)	405	3.0 Mm^{-1} 1.4 Mm^{-1}	11.7% (winter) 6.3% (fall)	PASS-3	Yuan et al. (2016a)
Nov. 2014	Heshan (China)	405	3.9 Mm^{-1}	12.1%	PASS-3	Yuan et al. (2016a)
Nov. 2016– Dec. 2016	Beijing (China)	370	106.4 Mm^{-1} 93.8 Mm^{-1}	46% (at the ground) 48% (at 260 m)	Aethalometer AE-33	Xie et al. (2018)
Jun. 2013 – May. 2016	Nanjing (China)	370	35.8 Mm^{-1}	16.7%	Aethalometer AE-31	Wang et al. (2018)
Jan. 2012	Nagoya (Japan)	405	Not detected	11% (300°C) 17% (400°C)	Thermodenuder PASS-3	(Nakayama et al. (2015))

957
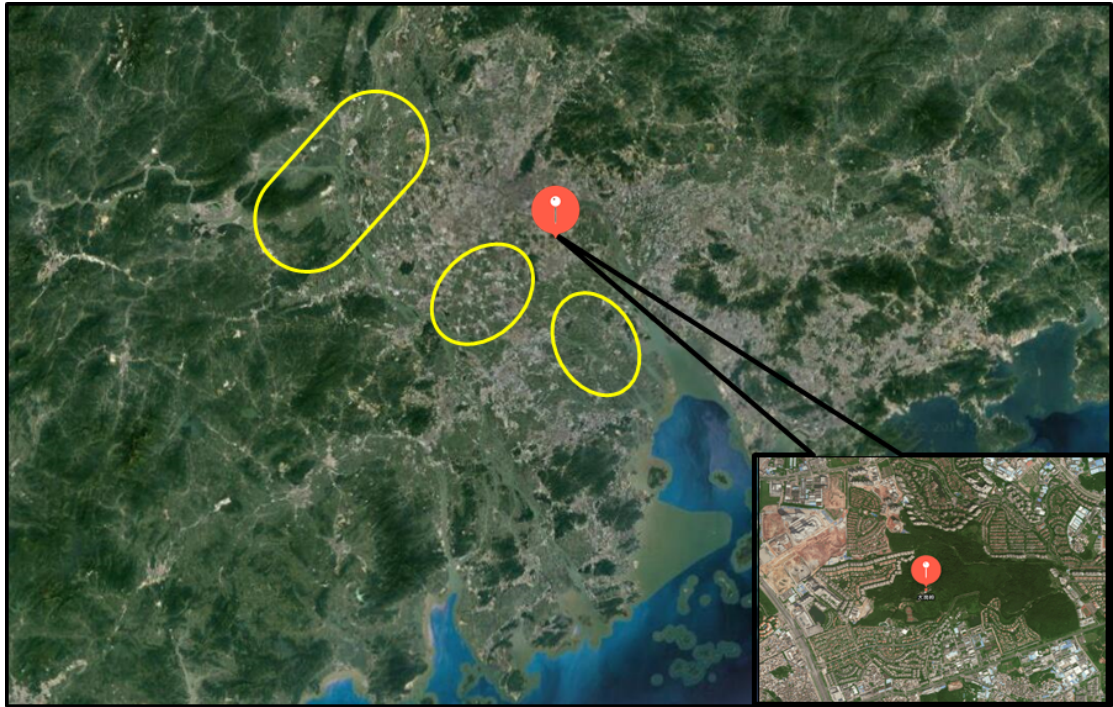
958

959 Figure 1. The location of Panyu station (CAWNET) in the PRD region (indicated by the red

960 dot). The plain areas within the yellow circles are the main rural areas of western PRD.

961

962
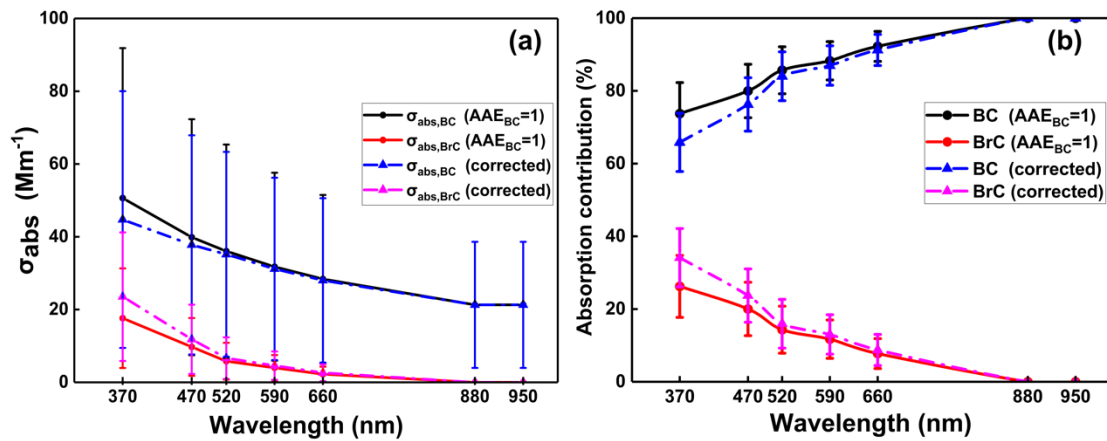
963

964 Figure 2. (a) BC and BrC particle average light absorption coefficients at different

965 wavelengths under different AAE_{BC} assumptions; the whiskers represent an error of

966 one standard deviation. (b) Contributions of BC and BrC to the total light absorption

967 coefficient at different wavelengths under different AAE_{BC} assumptions; the whiskers

968 represent an error of one standard deviation.

969
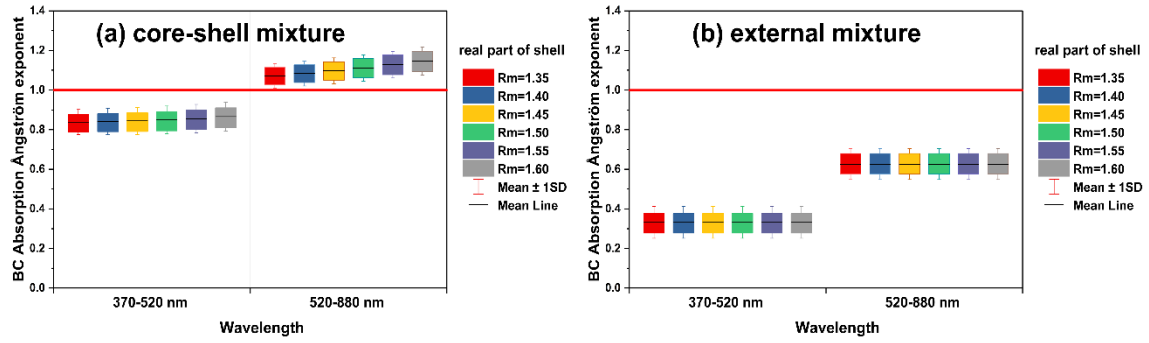
Figure 3. Influence of the wavelength-independent refractive index of the non-absorbing materials on the (a) AAEs of the core-shell mixture and (b) AAEs of the external mixture with a constant BC core refractive index ($\widetilde{m}_{core}=1.80-0.54i$). The imaginary part of the non(less)-absorbing shell was set to 10^{-7}, while the real part varied from 1.35 to1.60. In each panel, the boundaries of the box represent the 75th and 25th percentiles; the whiskers above and below each box indicate an error of one standard deviation; the black lines in the boxes denote the average values. In panels a and b, the red line indicates where $AAE_{BC}=1$.
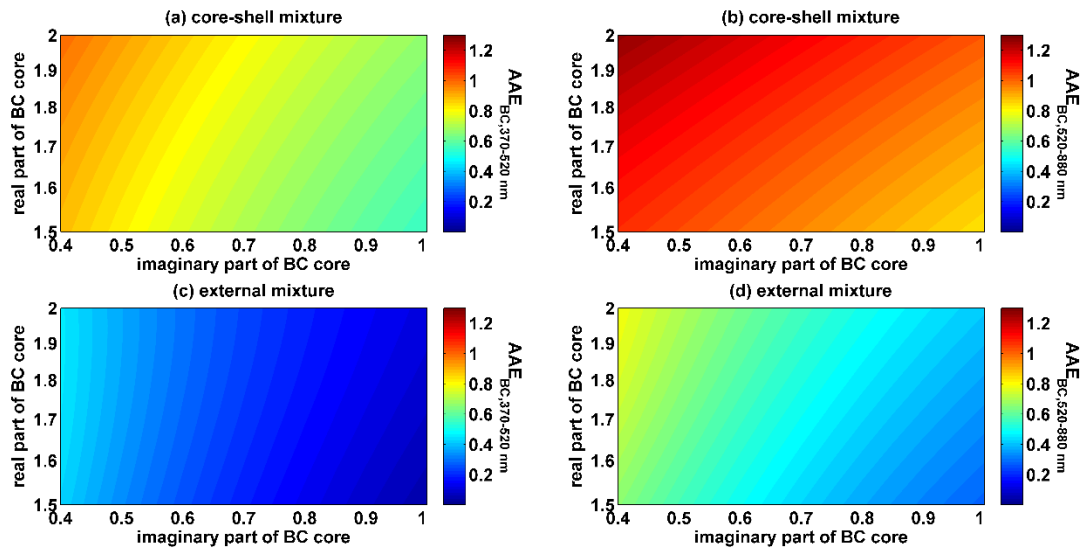
981 Figure 4. Influence of the wavelength-independent refractive index of the BC core on

982 AAEs with a constant shell refractive index ($\widetilde{m}_{shell}=1.55\text{-}10^{-7}i$). A core-shell mixture

983 was used for panels a and b, and an external mixture was used for panels c and d. The

984 real part of $\widetilde{m}_{core}$ varied from 1.5 to 2.0, with a step of 0.05, and the imaginary part of

985 $\widetilde{m}_{core}$ varied from 0.4 to 1.0, with a step of 0.05.

986
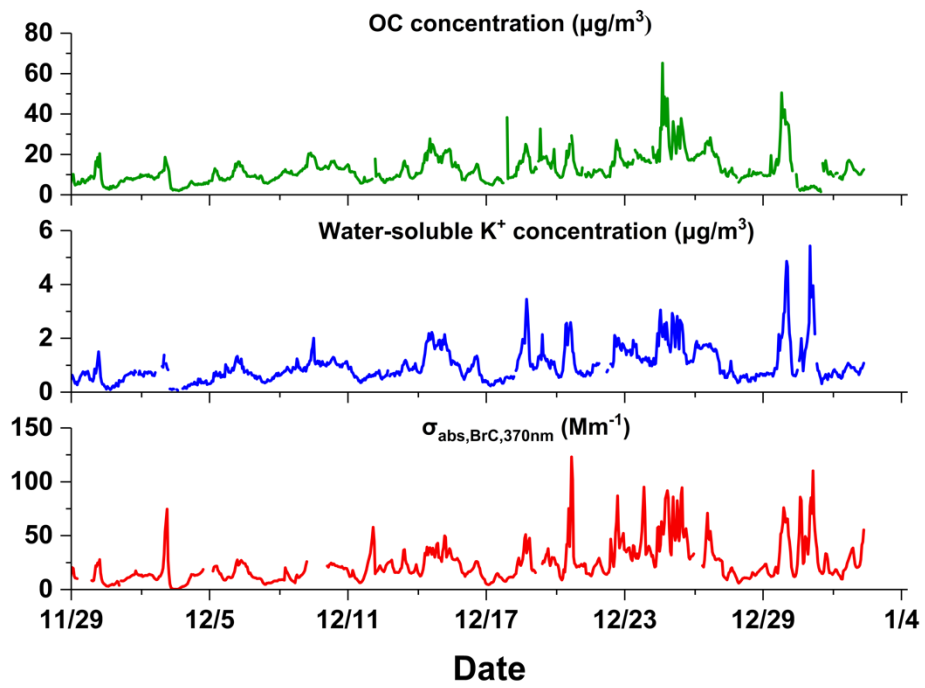
987

988   Figure 5. Time series of the OC aerosol mass concentration (green line), water-soluble K^{+} mass

989   concentration (blue line), and BrC light absorption (red line).

990
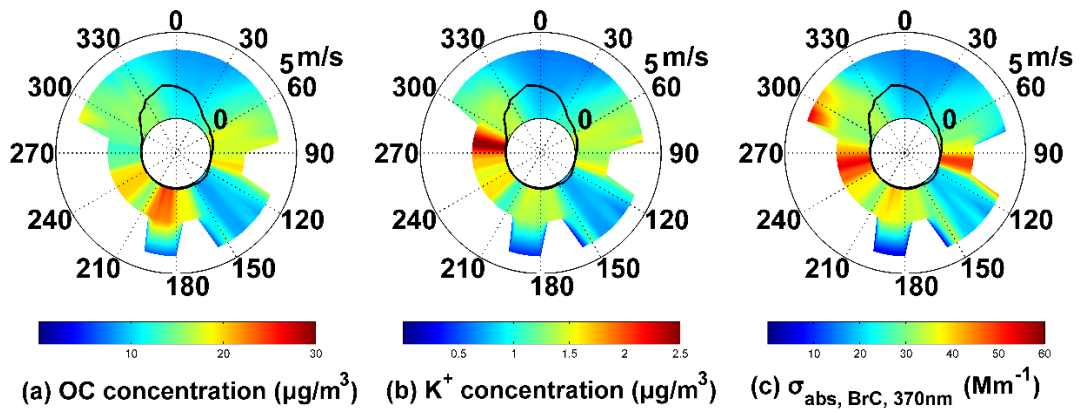
993 Figure 6. Wind rose plots of OC (a), K^{+} (b), and $\sigma_{abs,BrC,370nm}$ (c). In each panel, the black solid

994 lines denote the frequency of the wind direction. The shaded contour represents the average

995 values of the corresponding species for that wind speed (radial length) and wind direction

996 (transverse direction) in polar coordinates.

997

998
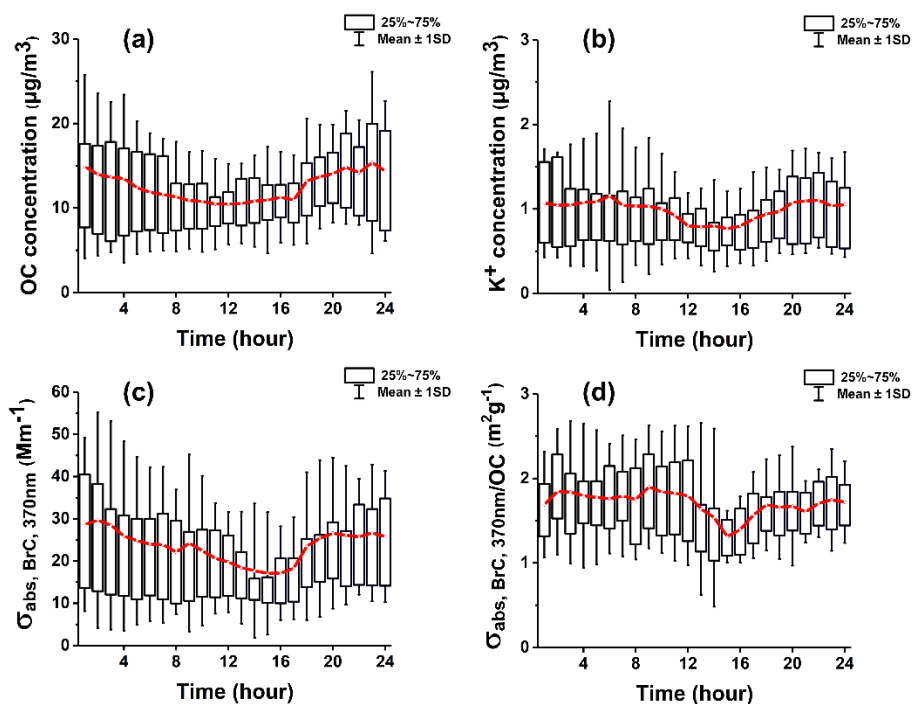
999

1000 Figure 7. Box-whisker plots of diurnal trends in the OC concentration (a), water-soluble K+

1001 concentration (b), $\sigma_{abs,BrC,370nm}$ (c), and $\sigma_{abs,BrC,370nm}$ /OC (d). The red traces represent the

1002 variation in the average value. The upper and lower boundaries of the box represent the 75th

1003 and 25th percentiles, respectively; the whiskers above and below each box represent an error

1004 of one standard deviation.

1005
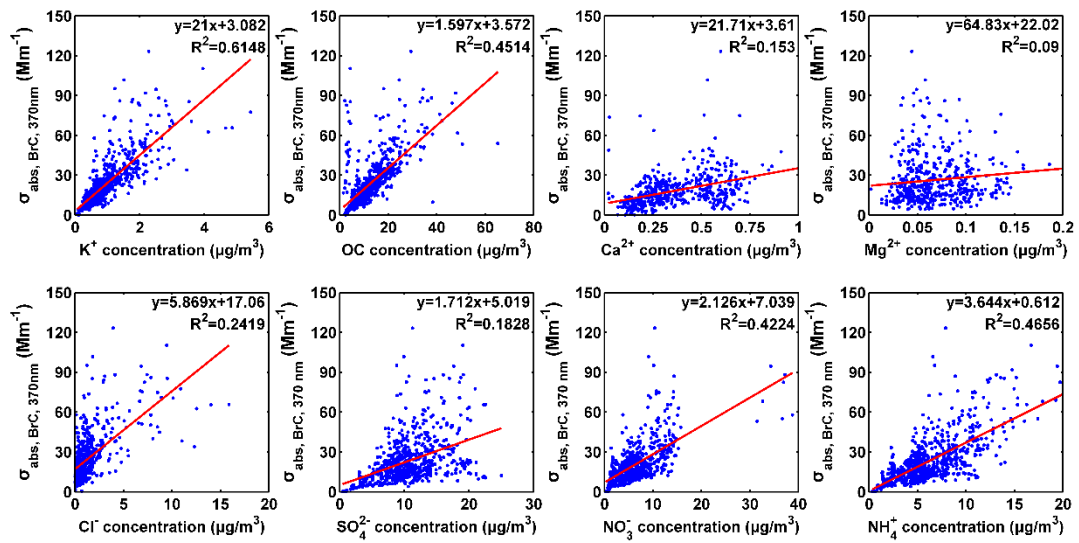
1006

1007   Figure 8. Correlations of the BrC absorption coefficient at 370 nm with OC, water-soluble K^+,

1008 Ca^{2+}, Mg^{2+}, Cl^-, SO_4^{2-}, NO_3^-, and NH_4^+ aerosol concentrations.
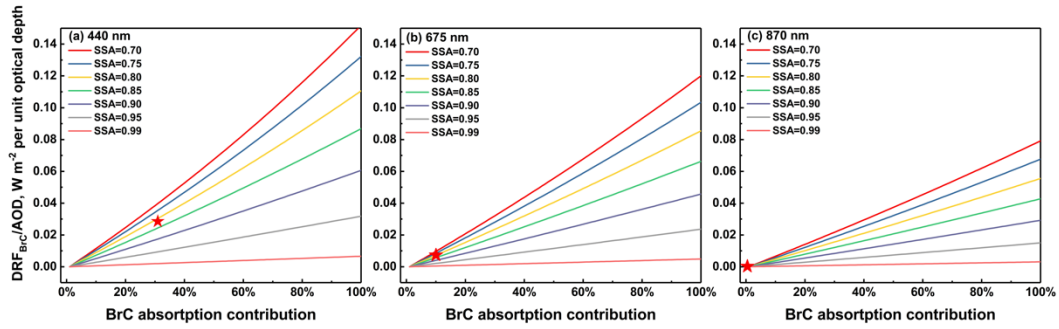
1009

1010 Figure 9. BrC radiative forcing efficiencies, which are defined as the BrC TOA direct radiative

1011 forcing divided by the AOD, as a function of the BrC to BC absorption ratio and *SSA* measured

1012 at the surface. The average AOD of the three wavelengths, the average ASY of the three

1013 wavelengths, a solar zenith angle of 55°, and average shortwave broadband surface albedo were

1014 used in the calculation. The red star corresponds to the average *SSA* and BrC absorption

1015 contributions determined from this campaign.